Journal of Structural Geology 164 (2022) 104730

Contents lists available at ScienceDirect

Journal of Structural Geology

journal homepage: www.elsevier.com/locate/jsg

Crystallographic and shape preferred orientation producing anisotropy in slates from Northern Spain

H.-R. Wenk [a,*], J. Huang [a,b], M. Devoe [a], J. Gómez-Barreiro [c], R. Vasin [d], Y. Ren [e,f], S. Barrios-Sánchez [c]

[a] Department of Earth and Planetary Science, University of California, Berkeley, CA, USA
[b] Department of Earth Science, Institute of Disaster Prevention, Yanjiao, Sanhe, Hebei Province, PR China
[c] Dpto. de Geologia, University of Salamanca, Salamanca, Spain
[d] Joint Institute for Nuclear Research, Frank Laboratory of Neutron Physics, Dubna, Russia
[e] Advanced Photon Source, Argonne National Laboratory, Lemont, IL, USA
[f] Department of Physics, City University of Hong Kong, Kowloon, Hong Kong

ARTICLE INFO

Keywords:
Slate
Microstructure
Crystallographic and shape preferred orientation
Seismic anisotropy
Northern Spain

ABSTRACT

Slates are common metasedimentary rocks in the Iberian Peninsula, ranging in deposition age from Proterozoic to Ordovician. Spain is currently the primary producer of high-quality slate products. The excellent cleavage is related to microstructures with very strong preferred orientation of white mica and chlorite. In this study we explore preferred orientation of eleven slates and one phyllite of different composition and metamorphic grade from Northern Spain with high energy synchrotron X-ray diffraction and study microstructures with scanning electron microscopy. While phyllosilicates display high crystallographic and shape preferred orientation, quartz, with also highly flattened grains, has in most samples a random crystallographic orientation. The microstructural and texture data are used to model anisotropic seismic properties with a self-consistent method and to explore the influence of crystal shapes on elastic anisotropy. Anisotropy for these slates is very high compared with gneiss and shale and, due to its prevalence, slate anisotropy contributes significantly to seismic anisotropy in the upper crust.

1. Introduction

Slates are remarkable metamorphic rocks with strong planar cleavage that extends over large distances. Such strong cleavage allows the preparation of plates several millimeters in thickness that can be used for roofs, floors and walls. We originally became fascinated with slates when we analyzed preferred orientation of a slate from the Belgian Ardennes and documented a texture strength of mica with over 100 multiples of random distribution (Wenk et al., 2019). This exceeds the textures of most materials, including rolled metal foils and recrystallized metals (Hutchinson and Nes, 1992). The discovery is even more remarkable since slates are fine-grained polyphase materials, generally composed of white mica, chlorite, quartz and accessories, compared to single phase metals.

The history of slate crystallographic preferred orientation (CPO), which was very popular in the 1970s, was reviewed by Wenk et al. (2020). The unique cleavage properties of slate caught early the attention of geologists who investigated slates and slaty cleavage first with optical microscopy (e.g. Sorby, 1853, 1856; Dieterich, 1969; Siddans, 1972; Wood, 1974; Means, 1981; Weber, 1981) and later with electron microscopy (e.g. Oertel and Phakey, 1972; Oertel et al., 1973; Knipe and White, 1977; White and Knipe, 1978), conventional X-ray pole figure goniometry (e.g. Oertel, 1983) and recently with electron backscattered diffraction (EBSD; e.g. Cárdenes et al., 2021).

Wenk et al. (2020) investigated mineral CPOs in randomly selected slate samples with high energy synchrotron X-ray diffraction and observed that extremely high CPO is not unique to Ardennes slates but similar textures are observed in a wide range of geological settings. While phyllosilicates display extreme CPO, surprisingly most quartz CPO, in spite of highly flattened oriented grains (shape preferred orientation, SPO), is practically random. Slates transformed from shales that underwent metamorphism and recrystallization. In shales, cleavage is parallel to the bedding plane formed during sedimentation and compaction. The slaty cleavage characteristic of slates is a secondary

* Corresponding author.
E-mail address: wenk@berkeley.edu (H.-R. Wenk).

https://doi.org/10.1016/j.jsg.2022.104730
Received 9 February 2022; Received in revised form 15 September 2022; Accepted 20 September 2022
Available online 25 September 2022

tectonic fabric developing at low-grade metamorphic conditions in argillaceous rocks. It reflects the finite strain that these rocks have undergone (e.g. Siddans, 1972; Wood, 1974; Williams, 1977 for overviews). The slaty cleavage primarily represents a compressive strain, with the phyllosilicate platelets oriented perpendicular to the principal shortening direction.

The strong CPO of phyllosilicates in low-grade metasediments is typically the result of regional deformation and could define a pervasive foliation over tens and hundreds of kilometers in orogenic belts (e.g. Wood and Oertel, 1980; Pérez-Estaún et al., 1991; Goldstein et al., 1998; van Norden et al., 2007; Turnbull et al., 2001; Herbosch et al., 2020) including the famous slate belt in Taiwan (Tillman and Byrne, 1995; Chen et al., 2019). This results in strong anisotropy of elastic properties which, in many cases, is significant for interpreting seismic anisotropy in the crust (e.g. Christensen and Mooney, 1965; Brocher and Christensen, 1990; Godfrey et al., 2000; Guo et al., 2014; Ji et al., 2015). Anisotropy is not only expressed in elastic properties but also in the magnetic signature (Haerinck et al., 2015).

Wenk et al. (2019, 2020) have optimized and standardized experimental techniques and methods of data analysis. It turns out that classical methods such as X-ray pole figure goniometry provide only qualitative information about CPO in slates, largely due to distortions of peak shape, particularly in reflection geometry, that cannot be corrected for extreme CPO (e.g. Wenk, 1998, p. 143). Comparatively, with high energy synchrotron diffraction methods the documented alignment of phyllosilicates is 5–10 times higher. Other techniques like EBSD tend to underestimate phyllosilicate contents because some diffraction patterns cannot be indexed, resulting in a biased quantification of CPO (e.g. Cárdenes et al., 2021). This inspired us to conduct a systematic study of slate CPO using synchrotron diffraction, focusing on slates from the Iberian Peninsula which has gained the reputation as the most important place in the world for industrially produced slates (Cárdenes et al., 2019) and very little is known about the microstructure and texture of slates from this region.

So far there have been no studies to document the individual influences of both crystallographic orientation and grain shape on elastic properties. Slates and phyllites with elastically highly anisotropic phyllosilicate crystals provide a unique opportunity to investigate the influence of anisotropic shapes and strong preferred orientation on seismic anisotropy.

2. Geological context and sample locations

In this study we have investigated low grade metasediments, mainly slates, from three different zones of the Variscan belt in the Iberian Massif (Fig. 1a). The Variscan orogen developed during the collision of Gondwana and Laurasia in the Paleozoic between 370 and 290 Ma (Azor et al., 2019). The geology of the Iberian Massif is characterized by an autochthonous Gondwanan domain overlain by an allochthon, which consists of a stack of peri-Gondwanan terranes and ophiolites (Gómez Barreiro et al., 2007). The Variscan Iberian Massif can be divided into six different zones (Fig. 1a). Allochthon and parautochthon are included in the Galicia-Tras-os-Montes Zone (GTMZ) which represents the most internal part of the orogen. It is surrounded by the Central Iberian Zone (CIZ), the eastern portion of which, the Ossa-Morena Zone (OMZ), is underlain by the West Asturian-Leonese Zone (WALZ) and the Cantabrian Zone (CZ), both of which represent the Variscan foreland (Julivert et al., 1972; Martínez Catalán et al., 2014). The OMZ is a slate belt similar to the CIZ but with some differences in terms of structural and stratigraphic evolution. The SPZ is a Variscan foredeep basin, dominated by thrust tectonics.

The structural evolution across the Iberian Massif includes contractional and extensional pulses related to plate convergence and gravitational re-equilibration. The first contractional events produced overturned and recumbent folds followed by the development of major thrusts and resulted in crustal thickening, which eventually led to extensional collapse and the formation of gneissic domes through the accumulation of ductile migmatites (Gómez Barreiro et al., 2010; Martínez Catalán et al., 2014). This is followed by a late-orogenic stage of vertical folding (Azor et al., 2019).

Here eleven slates and one phyllite have been investigated (Fig. 1, Table 1 and for sample locations Supplementary Table S1). Regional field evidence indicates that the samples represent low-grade metapelites extending over many kilometers and showing thousands of meters in thickness (e.g. Pérez-Estaún et al., 1991; Díez Balda et al., 1990).

2.1. Middle-Upper Ordovician - Ollo de Sapo Domain (CIZ)

Nine samples (Bv, Fo, Heb, Piv) were collected in the Truchas syncline area (Fig. 1c) of the Ollo de Sapo Domain in the CIZ (Fig. 1a). This is one of the most important areas for roofing slate production in the world with a production of more than 20,000 tons per year (Cárdenes et al., 2014). Roofing slates require large volumes of homogeneous material with minimal presence of secondary foliations, crenulations, veins and fractures, which reduce slate fissility (Cárdenes et al., 2014). As an aerial image demonstrates (Suppl. Fig. 1), there are many roofing slate quarries in this area what makes this area a world-class lithotech (Cárdenes et al., 2019).

The Truchas syncline is located in the CIZ (Fig. 1c). It is a Variscan synclinorium (Martínez Catalán et al., 1992) formed by several recumbent folds during the first contractional phase. The structure was refolded during the last contractional stage (Martínez Catalán et al., 2014; Azor et al., 2019). Regional metamorphism in the Truchas syncline is low-grade, being related to the Variscan deformation. Previous studies indicate low greenschist facies conditions (chlorite zone; 300-400 °C; García-Guinea et al., 1997).

Samples were collected in different quarries of Middle and Upper Ordovician slates (Table 1) in the Luarca and Rozadáis Formations (Fig. 1b). Fo samples come from normal limbs of recumbent folds (e.g. Fig. 2) and a penetrative slaty cleavage dominates the fabric. Bedding is recognized at outcrop scale, defined by silty beds. Sample Fo3 is very homogeneous with a barely visible cleavage in hand specimens (Fig. 3a). We will later see that this sample has a very low quartz content. In other samples bedding and cleavage planes are easily recognized, ranging between 0 and 10°, except for Fo8 with 20° (Fig. 3b).

The intersection of bedding and cleavage planes results in a linear structure which has been used as a reference for defining a coordinate system with X parallel to the lineation, Z perpendicular to the cleavage, and Y perpendicular to X and Z (e.g. for Fo9 in Fig. 4a).

Sample Piv1 (Fig. 4b) is a homogeneous black slate with an excellent slaty cleavage which comes from the Luarca Formation (Barrois, 1882). This formation is a stratigraphic succession of black/grey lutitic slates, depending on the organic matter content, with sporadic sandy interlays on the centimeter scale and some volcanic rocks on top (Barros Lorenzo, 1989). Shales were deposited during the Oretanian (470-457 Ma) in a graben basin along the Northern Gondwana continental margin under anoxic to euxinic conditions (Martínez Catalán et al., 1992). They were transformed into slates during the Variscan orogeny.

The Casaio, Rozadáis and Losadilla Formations represent the Upper Ordovician in the Truchas syncline, consisting of slates, sandstones and quartzites (Fig. 1c). We have collected samples at different levels of the Rozadáis Formation. This is a slaty sequence with dark-grey and black slates (lower section) evolving into silty slates with interlayered sandstones, quartzites and diamictites (upper section) (Gutiérrez-Marco et al., 2002). Samples Bv5a, Fo4, Fo9 and Heb1 are typical black slates with a visible lineation and a diffuse light-grey banding defining the bedding plane (e.g. Fig. 4a). Samples Fo2, Fo7 and Fo8 range from black to dark-grey slates.

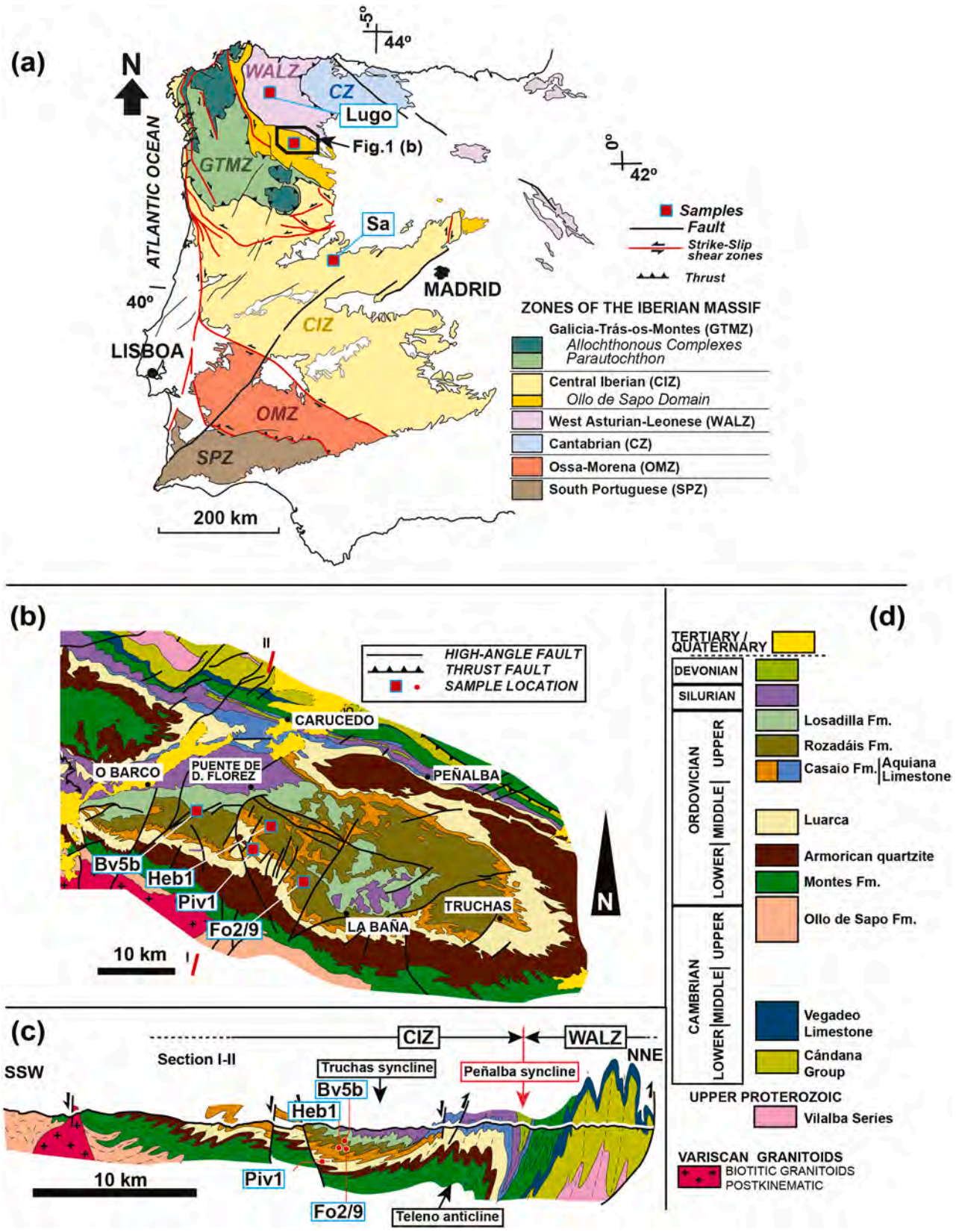

Fig. 1. (a) Geological map of the Variscan orogen in the Iberian Peninsula. Samples were collected in three different domains: Sa1 in Schist-Greywacke Complex (SGC) which is a part of the Central Iberian Zone (CIZ), Lugo1 in Mondoñedo Nappe of WALZ domain and Bv, Fo, Heb, and Piv in the Ollo de Sapo domain. The location of the studied areas (red squares) is indicated. The zones of the Variscan Iberian Massif and major faults and strike-slip shear zones are highlighted (after Martínez Catalán et al., 2014). (b) Geological map of the Truchas syncline and surrounding areas. (c) Geological section (I-II shown in (b)), with horizontal and vertical scales equal. Dashed lines represent axial planes of recumbent folds. Red squares: locations of the samples. d) Stratigraphic legend and ages (after Gutiérrez-Marco et al., 2019).

Table 1
Samples and geological settings same format as for the rest.

Sample	Lithology	Unit	Age	Variscan Domain	Metamorphic grade		References
Bv5b Fo2 Fo3 Fo4 Fo7 Fo8a Fo8b Fo9 Heb1	black slate	Rozadáis	Upper Ordovician	Ollo de Sapo (Truchas syncline)	Greenschist facies (Chlorite zone)	300-400 °C	Cárdenes et al. (2014) Barros Lorenzo (1989) García Guinéa et al. (1997)
Piv1	black slate	Luarca	Middle Ordovician				
Lugo1	green slate	Cándana Slates	Lower Cambrian	Mondoñedo Nappe	Greenschist facies (Biotite zone)	<450 °C	González Lodeiro et al. (1979) Cárdenes et al. (2014)
Sa1	phyllite	Monterrubio	Upper Proterozoic	Schist-Greywacke Complex			Díez Balda et al. (1995)

Fig. 2. Detail of the Os Follos quarry, where most of the Fo samples were collected (see Fig. 1c for locality, view is NW). Slate extraction is focused on the lower part of the quarry (black slates level) just below the Os Follos quartzite (Barros Lorenzo, 1989) with minor folds. The quartzite marks the bedding plane. Slaty cleavage is indicated with dashed white lines.

2.2. Lower Cambrian - Mondoñedo Nappe Domain (WALZ)

The sample Lugo1 comes from the Cándana Group (Lower Cambrian; Terra Chá-Lorixe quarry). The area is a part of the Mondoñedo Nappe Domain in the WALZ. The Cándana slates in this area have a thickness of 500 m, with schists and carbonates also present. The sample Lugo1, a high quality roofing slate, comes from the upper section with ca. 200 m of green to greenish-grey slates (Fig. 4c). The fissility grade of this slate is relatively low (Cárdenes et al., 2013). The original sediments of the Cándana Group were deposited under shallow marine conditions. Variscan regional metamorphism transformed the original shales into slates and phyllites. The mineral assemblage includes quartz, white mica (muscovite), chlorite and minor biotite suggesting metamorphic conditions ~450 °C (Cárdenes et al., 2013). The structure in the area is complex with overturned and recumbent N–S folds with an axial planar foliation (300–335 Ma; Dallmeyer et al., 1997) (Suppl. Fig. 2), and relatively open, upright folds with a similar trend, and local development of cleavage in a cartographic interference patterns (González Lodeiro et al., 1979; Martínez Catalán et al., 2014).

2.3. Upper Proterozoic-Lower Cambrian - the Schist-Greywacke Complex (CIZ)

Sample Sa1 is a phyllite, not a slate, and was collected from the Schist-Greywacke Complex (SGC) in Salvatierra de Tórmes (Salamanca) in the CIZ (Table 1, Suppl. Fig. 3). We use this sample to highlight the different microstructures in pelitic metamorphic rocks. It belongs to the lower section of the SGC in the Monterrubio Formation, which consists of more than 2000 m of metapelites with thin interbedded layers of sandstones, vulcanites and conglomerates (Díez Balda et al., 1990). Sample Sa1 was collected between the biotite and almandine Barrovian isograds (<450 °C) and shows a penetrative crenulation cleavage (Fig. 3c). Original shales were deposited in a slope-distributary channel complex in the context of the Iapetus ocean. Metamorphic

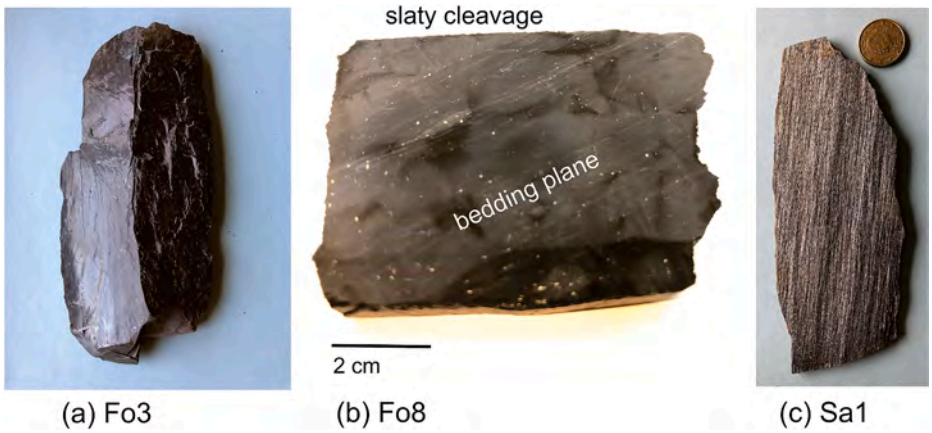

Fig. 3. Hand specimens of slates. (a) Fo3 with no quartz, (b) Fo8 with diagonal bedding and slaty cleavage (horizontal), (c) phyllite Sa1 with crenulation lineation. Scale (2 cm) applies to all.

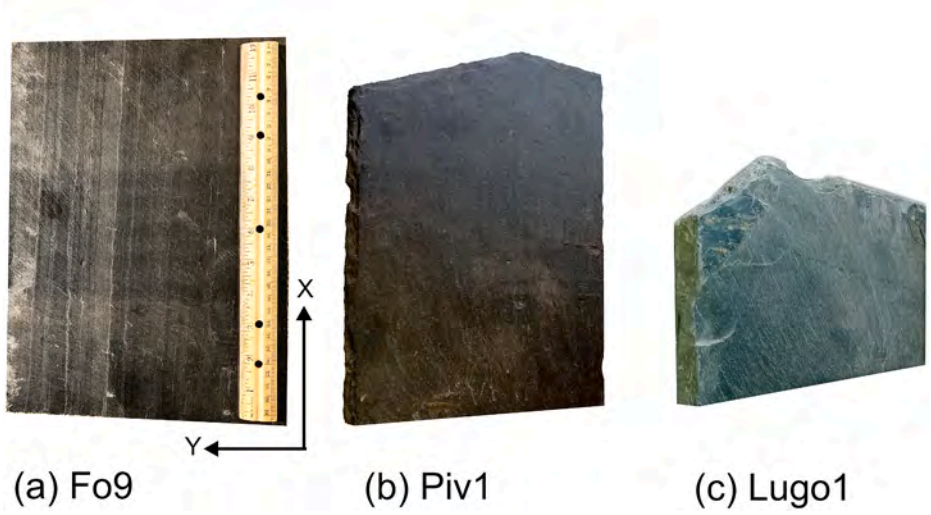

Fig. 4. Roofing slates: (a) Fo9, Os Follos black slate with visible vertical lineation (1st. quality tiles). (b) Piv1, Luarca Fm. black slate. These slates are very homogeneous. (c) Lugo1, Green Lugo slate. In all cases, tile width is 21 cm, thickness varies from 2.5 mm (Fo9), 5 mm (Piv1) to 9 mm (Lugo1). Scale is 30 cm. XY coordinates are indicated. (For interpretation of the references to color in this figure legend, the reader is referred to the Web version of this article.)

transformation of the shale into a phyllite occurred during the Variscan Orogeny. Contractional phases led to a Barrovian metamorphism (360-320 Ma) with peak pressure conditions of 400–550 MPa and temperature conditions greater than 650 °C (Díez Balda et al., 1995; Azor et al., 2019).

3. Microstructures and mineral composition investigated with SEM

From hand specimens polished 30 μm thin sections were prepared perpendicular to the slaty cleavage and assigned coordinates: Z perpendicular to the cleavage, X parallel to the lineation and Y perpendicular to X and Z (Fig. 4a). Because of the fine grain size optical microscopy with a petrographic microscope is not very informative. Therefore microstructures were analyzed with scanning electron microscopy (SEM). Carbon-coated thin sections were analyzed with a Zeiss-EVO scanning electron microscope in high vacuum mode at 20 kV and a beam current of 2 nA. We mainly used backscatter electron (BSE) detectors for imaging where the brightness of each phase imaged is dominantly related to their respective atomic number, making it easy to identify the main components in the samples: chlorite (bright), white mica (muscovite/illite) (light grey) and quartz (darker grey) (Fig. 5a and b). In the transition from shale to slate and schist, illite-smectite transforms to white mica and chlorite but, as we will see, this transition is not quite complete in slates. Thus we will use the name “white mica” in most of this paper.

SEM-BSE images for Lugo1 clearly document a different shape for chlorite, white mica, as well as quartz, parallel (Fig. 5a) and perpendicular to the lineation (Fig. 5b). From such images the grain shape can be estimated by measuring the longest and shortest axes of each grain, assuming an ellipsoidal shape (Fig. 6). This was done manually on ten grains per sample to determine an average length/width ratio in XZ sections (Table 2). For Lugo1 XZ (Fig. 5a) the average ratios for white mica are ~16, for chlorite ~15 and for quartz ~8. In YZ sections (Fig. 5b) they are ~7.6, ~7.5 and ~4.5, respectively. Overall aspect ratios of phyllosilicates as well as quartz are about two times larger parallel than perpendicular to the lineation.

With energy-dispersive spectroscopy (EDS) and an EDAX-AMETEK detector and analytical software, phases were identified (Table 2) and chemical composition was estimated for white mica (Table S2) and chlorite (Table S4).

SEM-BSE images for all samples are presented in Fig. 7 and some details are highlighted in Fig. 8. Grain alignment is most regular in Bv5b, Fo3, Fo4, Piv1 and Lugo1. All images in Fig. 7 are XZ sections (parallel to the lineation), except Sa1 (Fig. 7k) which is perpendicular to the lineation (YZ). Grain size is similar in slates sampled from the same location.

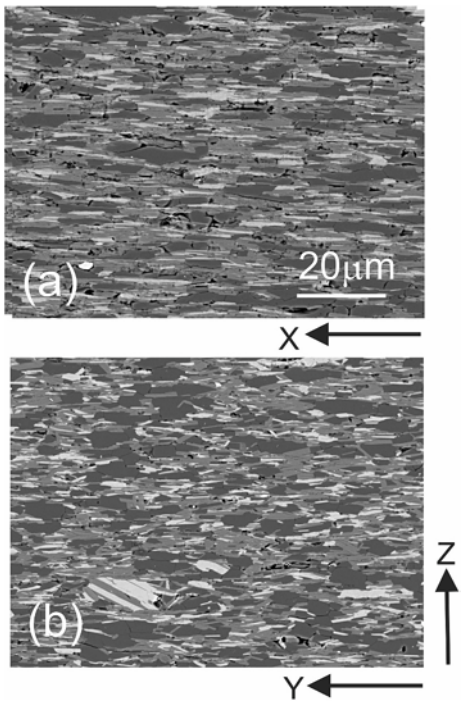

Fig. 5. SEM-BSE microstructural images of slate Lugo1. Quartz is dark, chlorite is bright and white mica is light grey. (a) is parallel to the lineation (X) where grains have a larger aspect ratio (length/width), and (b) perpendicular to the lineation (Y) with a smaller aspect ratio.

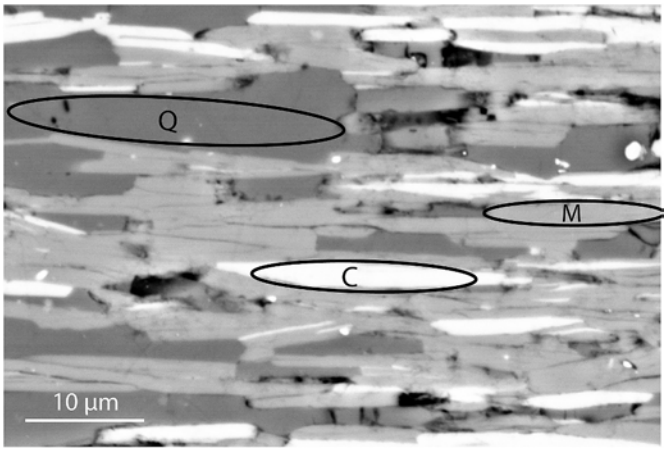

Fig. 6. SEM-BSE image of microstructure in Fo9 with chlorite (C), white mica (M) and quartz (Q). Ellipses approximate grain shapes and averages over 10 grains (Table 2). They are used in GeoMixSelf to calculate aggregate elastic properties (Table 4).

On average, phyllosilicate sizes within a sample range from 5 to 20 μm in length and 1–3 μm in width. All Fo samples show an average for phyllosilicates 10 μm in length and 1 μm in width and for quartz around 12 μm in length and 3 μm in width in XZ sections. The largest grains are found in slate sample Bv5b with phyllosilicates average in length 20 μm and 2 μm in width (Fig. 7a) and phyllite Sa1 with crystals up to 50 μm in size (Fig. 7k). The smallest grains are in Piv1 with phyllosilicates averaging 7 μm in length and 2 μm in width (Fig. 7i). The aspect ratios of phyllosilicates in XZ sections average to 1:10, but are slightly less for Fo7 and Fo9 (Table 2). Fo9 shows occasional kink bands (Fig. 8d).

The phyllite Sa1 from Salvatierra de Tormes shows a more complex microstructure than slates, with a clear crenulation cleavage (Fig. 8g). The macroscopic foliation corresponds to a crenulation cleavage (S3, in Fig. 8g). Two types of layers are recognized: the cleavage domains with undulating fine-grained white mica, some chlorite and occasional biotite (B), and much coarser quartz-rich microlithon layers, where relics of an older foliation (S1) appear (Fig. 8 g-i) (Passchier and Trouw, 2005, p. 366). Phyllosilicates in the fine-grained mica-rich domains, defining the S3 foliation, are more or less perpendicular to those in the quartz-rich layers, which define the S1 foliation. We will see that this is also expressed in the preferred orientation patterns.

Quartz grains are also flat in most samples, except Sa1 and Fo7, with an aspect ratio ~1:5 (Figs. 7 and 8, Table 2). Sample Fo3 has practically no quartz. While most phyllosilicates are horizontally aligned parallel to the cleavage, there are some exceptions of chlorite-white mica stacks that are oriented oblique to the cleavage direction (e.g. Fo4, Fig. 7d; Piv1, Fig. 7i; Fo3, Fig. 8a; Heb1, Fig. 8e). Such stacking makes quantitative EDS analysis difficult because the beam penetrates into the sample and averages (e.g. Kisch, 1990). These stacks have aspect ratios of ~ 1–3.

SEM-BSE images clearly display accessories, many with high brightness. They were identified with EDS analyses. Apatite has a prismatic shape and the prisms are more or less aligned parallel to the cleavage plane (Ap in Fo9, Fig. 7g; Fo3, Fig. 8b). In some samples there are large crystals of monazite showing late-kinematic relationships (Mo, e.g. Fo3, Fig. 7c; Fo9, Fig. 8c). In Lugo1 there are large secondary crystals of ilmenite (Fig. 8f). Only in Sa1 could we identify relatively large crystals of biotite (Fig. 8g).

Based on EDS analyses, white mica in all samples is basically muscovite but with minor components of Mg and Fe (Supplementary Table S2). This could be due to submicroscopic interlayers of chlorite (e.g. Fig. 8a, e) or incomplete transformation from illite/phengite (e.g. Minato and Takano, 1952). All chlorites have a high iron content (Fe/Mg~1.6) (Table S4). Compositional variations of white mica and chlorite are minor. Note that our EDS analyses are semi-quantitative but atomic proportions are very consistent.

4. Crystallographic preferred orientation and volume fractions measured with high energy synchrotron X-ray diffraction

Crystallographic preferred orientation (CPO) of fine-grained slates can be measured quantitatively with high energy X-ray diffraction on bulk samples and electron backscatter diffraction (EBSD) on single grains with scanning electron microscopy. Examples of the two methods were discussed in a review and compared with earlier qualitative results from X-ray pole figure goniometry (Wenk et al., 2020). Here we use high energy synchrotron X-rays which is an excellent method to quantify strong preferred orientation in fine-grained materials due to its ability to characterize bulk grain statistics with high sample penetration and low diffraction angles. All samples were prepared identically, measured with the same instrumental settings and diffraction data were analyzed with the same methods.

Rectangular prismatic blocks 3–5 mm wide and ~10 mm long were cut with a diamond saw using the sample XYZ reference system defined above. The long axis of the block (Z-axis) is perpendicular to the cleavage plane, and the perpendicular X-axis is parallel to the lineation. Then the long prism edges were ground down manually to an approximately cylindrical shape with its long Z axis perpendicular to the cleavage plane of the sample. This method was better than using a core-drill, which caused fracturing on the cleavage. The cylinders were then mounted on a metal rod and measured at the high energy beamline 11-ID-C of the Advanced Photon Source synchrotron at Argonne National Laboratory.

A schematic of the experiment is shown in Fig. 9. An X-ray beam with a wavelength of 0.1173 Å (105.7 keV) and a spot size of ~0.8 mm × 0.8 mm reaches the sample, which is mounted on a goniometer head with a horizontal rotation axis (laboratory Z-axis). The sample is tilted and translated on the goniometer head to bring the center of the cylinder

Table 2
Volume fraction of each mineral (in %) quantified by synchrotron X-ray diffraction, average aspect ratio (length/width averaged over 10 grains) for white mica, chlorite and quartz, and accessories (Ab albite, Ap apatite, Bi biotite, Ilm ilmenite, Mo monazite, Py pyrite, Ru rutile determined with scanning electron microscopy. Standard deviations of volume fractions in parentheses (last digit). Aspect ratios calculated from XZ sections.

	Volume fractions (%)				Aspect ratios (length/width)			Accessories
	White mica	Chlorite	Quartz	Albite	White mica	Chlorite	Quartz	
Bv5b	44.5(3)	24.1(2)	24.8(2)	6.5(4)	10	10	3	Ap, Ru
Fo2	38.4(1)	25.6(1)	25.6(1)	10.5(1)	10	7	3	Ap, Py, Ru
Fo3	63.5(6)	36.3(3)	0.1(5)	–	10	13	NA	Ab, Ap, Mo, Py, Ru
Fo4	41.3(2)	27.4(1)	22.1(1)	9.2(1)	8	7	4	Py, Ru
Fo7	45.0(1)	16.4(1)	34.1(1)	8.6(1)	8	5	3	Py, Ru
Fo8a	35.3(1)	26.3(1)	28.3(1)	10.1(1)	14	9	4	Mo, Ru
Fo8b	35.3(1)	26.3(1)	28.3(1)	10.1(1)	–	–	–	–
Fo9	38.9(2)	27.3(1)	26.7(1)	7.1(1)	7	6	3	Ap, Mo, Py,
Heb1	36.7(1)	29.9(1)	26.2(1)	7.2(1)	7	10	5	Ap, Py, Ru
Lugo1	40.2(1)	16.8(1)	42.9(1)	–	11	11	4	Ilm
Piv1	42.3(1)	26.0(1)	31.7(1)	–	10	10	3	Ap, Ru
Sa1	39.4(2)	19.7(1)	31.5(2)	9.4(5)	15	10	2	Ap, Bi, Ru

into the center of the beam and the cylinder axis parallel to the horizontal rotation axis. About 10 cm behind the sample the primary beam is captured by a beam stop. The diffraction images are recorded with a PerkinElmer 2D image plate detector mounted ≈195 cm from the sample.

The experiment takes advantage of the high energy of X-rays, not only for good sample penetration, but also for low diffraction angles (a range of $2\theta = 0.4–3.5^\circ$ was used, corresponding to lattice d-spacings 15.0 to 1.92 Å). Recorded diffraction peaks correspond to lattice planes that are barely tilted relative to the incoming X-ray ($\theta = 0.2–1.75^\circ$). Note that in the schematic Fig. 9 a much larger wavelength and corresponding larger 2θ is depicted for illustrative clarity.

Before measuring slate samples the instrument geometry is calibrated with a LaB_6 standard (a = 4.156468 Å) to refine sample-detector distance, exact detector orientation and instrumental resolution (Caglioti function, Caglioti et al., 1958). Slate samples were then measured over a φ 0–165° range, rotating around Z. During each rotation, 11 "composite" images at $\varphi = 15^\circ$ rotation intervals were acquired. A composite image is a sum over ~200 diffraction images captured using 0.5 s exposure during the rotation interval. During each rotation interval, the sample was also translated along the cylindrical axis (Z) to improve grain statistics. The measurement of a sample, including mounting of the sample, software control, φ-rotations and exposure time, takes about 20 min.

Two typical diffraction images for slates Fo3 and Fo4 are shown in Fig. 10. Each circular Debye ring represents diffraction from a different lattice plane *hkl*. Azimuthal intensity variations along the rings (η angle) indicate strong preferred orientation for white mica/muscovite and chlorite and minimal preferred orientation for quartz, the main mineral constituents in the sample Fo4 (Fig. 10b). Fo3 is exceptional, with almost no quartz (Fig. 10a). (00*l*) diffractions of phyllosilicates are strongest perpendicular to the vertical cleavage (horizontal direction Z in Fig. 10).

The 11 images at different φ-rotations in 15° intervals (from 0° to 165°) are then used to map the three-dimensional diffracted intensity distribution relative to sample coordinates XYZ, which can be projected on a pole figure (the insert in upper left of Fig. 9 shows a simplified pole figure coverage for 6 images at 30° φ-intervals). The rotation is about the axis normal to the cleavage plane (Z). There is good coverage of different directions with data, particularly the center which corresponds to (001) maximum of phyllosilicate pole figures.

The 11 diffraction images for a sample were then analyzed simultaneously with the Rietveld method (Rietveld, 1969), which relies on a least-squares fit to minimize the difference between experimental diffraction data and a calculated model that is based on diffractometer parameters, beam intensity, scattering background, crystal structures, crystal preferred orientations and volume fractions of components. For the Rietveld refinement the software MAUD was used (Lutterotti et al., 1997). Details on the software and routine analysis procedures are described in tutorials (Lutterotti et al., 2014; Wenk et al., 2014). First 2D images (Fig. 10) were integrated over 5° azimuthal sectors along the η angle to produce 72 conventional diffraction patterns. A total of $11 \times 72 = 792$ patterns for each sample, with 2θ ranging from 0.4° to 3.5°, were then used in the Rietveld refinement.

A polynomial function with five coefficients was used to refine the background of each image and 3–5 minerals were considered with corresponding crystallographic information from the literature: for white mica 2M-muscovite (Guggenheim et al., 1987, C2/c amcsd 0001076), trigonal quartz (Antao et al., 2008, $P3_121$ amcsd 0006212), and triclinic chlorite (Zanazzi et al., 2009, C-1 amcsd 0007298). We also tried monoclinic chlorite but the refinement quality was worse. Other minor phases such as biotite (Bohlen et al., 1980, C2/c amcsd 0000756), low albite (Winter et al., 1977, C-1 amcsd 0000715) and apatite (Hughes et al., 1989, $P6_3/m$ amcsd 0001259) were included for some samples. Note that for the texture analysis in MAUD, the first setting for monoclinic crystals such as white mica (muscovite) and biotite needs to be applied, i.e. (100) is the cleavage plane instead of the more familiar second setting with (001) as the cleavage plane (Matthies and Wenk, 2009). But for labels of lattice planes *hkl* in text, tables and figures we use the more conventional second setting.

A comparison of the calculated model (Fig. 11 "Fit") with experimental patterns (Fig. 11 "Measured") for sample Fo3 shows a close similarity, indicative of an excellent fit, both in positions as well as intensities of diffraction peaks. Parameters that were refined in the Rietveld analysis were scattering background, lattice parameters of phases (Supplementary Tables S3 and S5), size and shape of crystallites and microstrains (using the anisotropic Popa, 1998 model), crystal orientations as well as volume fractions of phases.

Most important for this study are three-dimensional crystallographic preferred orientation distribution functions (ODF) which are expressed in intensity variations along Debye rings. They were refined with the discrete EWIMV method, based on WIMV (Matthies and Vinel, 1982) but allowing for arbitrary data coverage. No sample symmetry was imposed and an ODF 7.5° cell size was considered for the discrete orientation space for every mineral. The refined ODF was then exported from MAUD and introduced into the BEARTEX software (Wenk et al., 1998) to rotate the sample orientation such that the normal to the cleavage plane (Z-axis) is in the pole figure center and, if there is a girdle-like distribution, the girdle is perpendicular to the X-axis of the pole figure, i.e. normal to the lineation. The transformed ODFs were then used to calculate and plot pole figures of minerals as well as to model bulk elastic properties of each sample.

The Rietveld refinement also provides quantitative information about phase volume fractions. The main phases in all samples are white

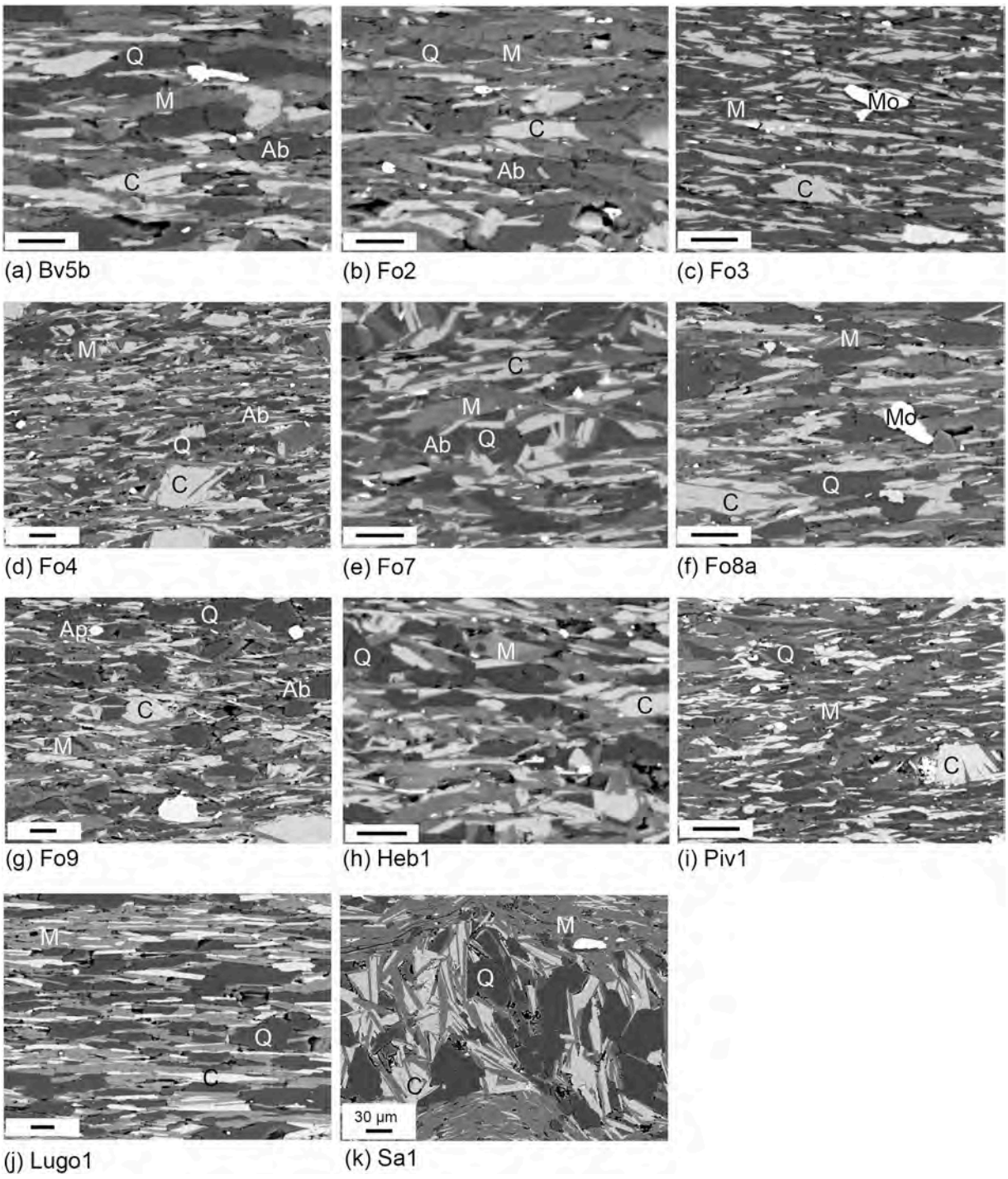

Fig. 7. (a–k). SEM-BSE images of slate samples cut perpendicular to cleavage and parallel to the lineation (XZ) except for (k) Sa1 which is perpendicular to the lineation (YZ). Phases identified using SEM-EDS and labeled as chlorite (C), white mica (M), quartz (Q), albite (Ab), apatite (Ap) and monazite (Mo). All scale bars are 10 μm unless otherwise labeled. Images were taken in high vacuum mode at a working distance of 15 mm and accelerating voltage of 20 kV.

mica, chlorite and quartz (Table 2). Lugo1 has the highest quartz content (42.9%). The quartz + albite content of black to dark-grey slates Fo2, Fo7 and Fo8 range from 36 to 43% and for Bv5b, Fo4, Fo9 and Heb1 it is less than 35%. Sample Fo3 is a homogeneous black slate with the lowest quartz + albite content (0.1%).

ODFs, as well as pole density values in pole figures are expressed in multiples of random distribution (mrd) with 1 mrd corresponding to an isotropic distribution (or absence of preferred orientation) and ∞ corresponding to a single crystal orientation. Pole figures are displayed for white mica (Fig. 12), chlorite (Fig. 13), quartz (Fig. 14), apatite (Fig. 15a) and biotite (Fig. 15b). Some information is summarized in Table 3. Pole figures are projected on the cleavage plane (XY) in equal area projections to produce minimal distortion of the dominant (001) maximum (in the center) and display deviations from axial symmetry.

For white mica the (001) pole figure maxima vary from 25 mrd to 120 mrd, for chlorite from 13 mrd to 125 mrd. The strongest preferred orientations are in Lugo1 (white mica 120 mrd and chlorite 125 mrd) and Fo4 (white mica 83 mrd, chlorite 84 mrd), and relatively weak orientations were observed in Fo2 (white mica 25 mrd, chlorite 22 mrd), Fo8 (white mica 29 mrd, chlorite 37 mrd) and Sa1 phyllite (white mica

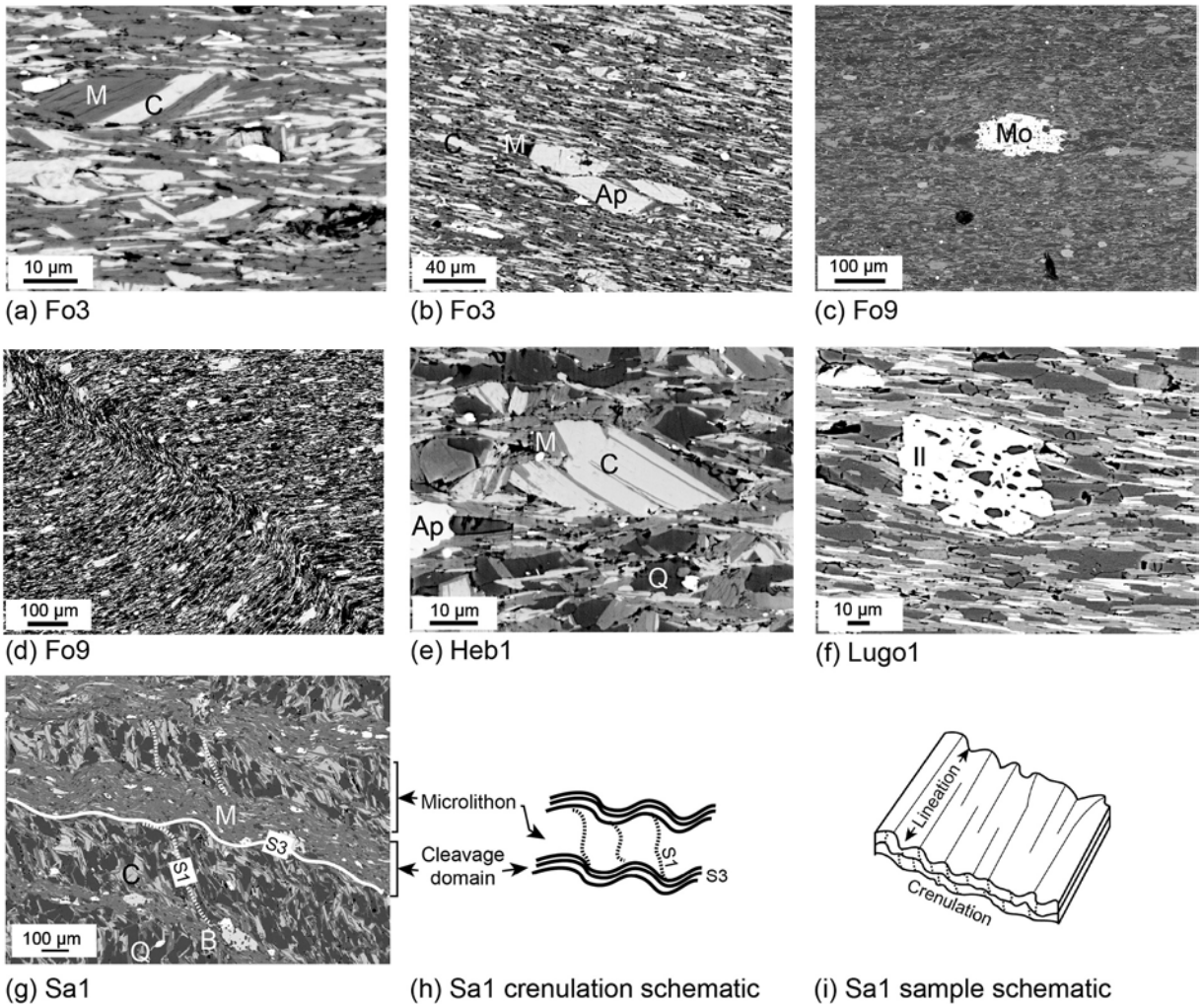

Fig. 8. (a–f). SEM-BSE images of details in some samples as discussed in the text. Phases identified using SEM-EDS are chlorite (C), white mica (M), quartz (Q), albite (Ab), apatite (Ap), biotite (B), ilmenite (Il) and monazite (Mo). (g–i) Some details about crenulation cleavage in phyllite Sa1. (g) There are different planar features: S1 (dotted line) is an older foliation, and S3 (white line) is the crenulation cleavage, which define the fissility of the rock. Note that a late crenulation of low amplitude overlaps S3. (h) Schematic outlining of microlithon and cleavage domain. The cleavage domain, predominantly composed of white mica, corresponds to a compressional foliation (S3). Within microlithons transposed relics of the S1 foliation are preserved. (i) 3D image with horizontal crenulation cleavage (S3) and late crenulation lineation (see also Fig. 3c).

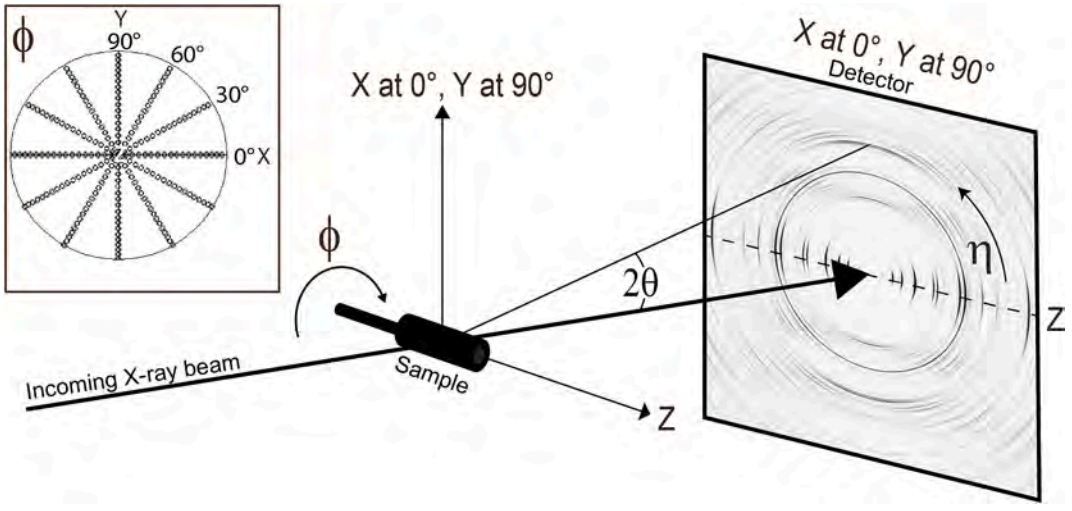

Fig. 9. Schematic of X-ray diffraction experiment with X-ray beam, cylindrical sample mounted on a goniometer head and incrementally rotated (φ) around Z, and detector with diffraction image. Upper left is the pole figure coverage with 6 images taken at different angles φ. Each dot represents a diffraction pattern averaged over 5° on η). Note that there is excellent coverage in the center (Z) for the main orientation maximum (001 of phyllosilicates).

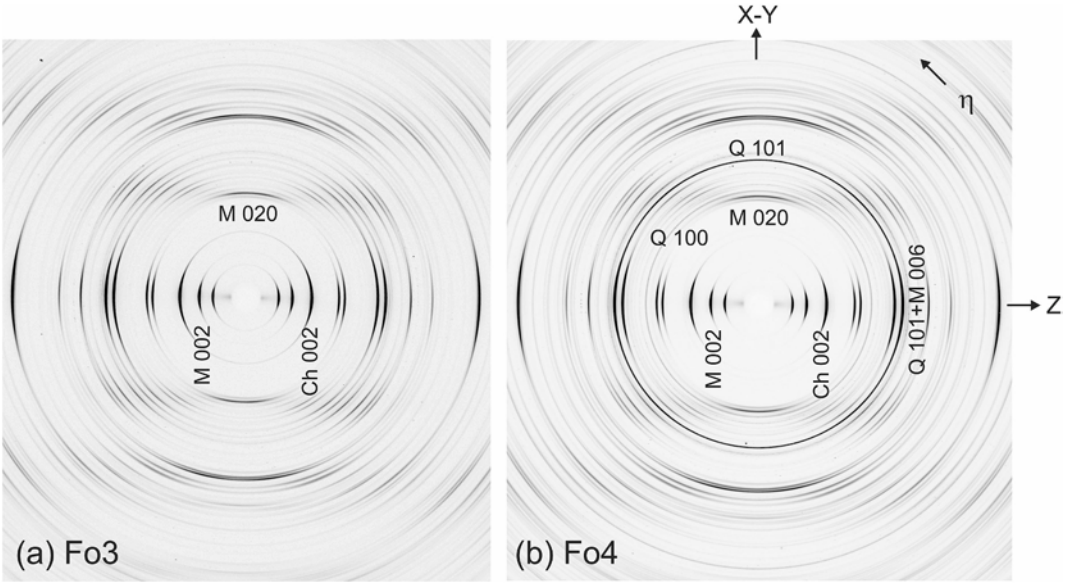

Fig. 10. Selected diffraction images for (a) Fo3 (without quartz) and (b) Fo4 (with quartz). Intensity variations along Debye rings are indicative of preferred orientation. In (b) for quartz 100 and 101=(101 + 011) there are no intensity variations and thus no CPO. Cleavage plane is vertical. Z is normal to cleavage (horizontal) and vertical axis varies between X and Y depending on sample rotation (φ); η defines the azimuthal angle of patterns on the Debye ring.

42 mrd, chlorite 14 mrd). In many samples white mica and chlorite show similar maxima, an exception is Sa1 where chlorite is much weaker which is consistent with the complex microstructure (Figs. 7k and 8g). All samples show a girdle in the YZ plane, most pronounced in Fo8, Fo9, Lugo1 and Sa1. In Fo3 and Piv1 the distributions are close to axial symmetry. Texture patterns for Sa1 reflect the crenulation cleavage, with a minor (001) sub-maximum in Y (both for chlorite and white mica), which correlates with the quartz-rich microlithon layers in Fig. 8g (S1).

In actual 3D ODFs exported from MAUD, ODF maxima are considerably higher than (001) pole figure maxima (Table 3) reaching 310 mrd for white mica and 951 mrd for chlorite in Lugo1. This is because 2D pole figures are 3D ODF projections. ODFs are used to calculate pole figures as well as anisotropic physical properties.

Perhaps most surprising has been the effective absence of significant preferred orientation for quartz (Fig. 14) in spite of the highly flattened grain shape as displayed in SEM images (Fig. 7). Except for phyllite Sa1 with fairly equiaxed quartz, aspect ratios range from 3 to 5 (Table 2). Pole figure maxima for quartz range from 1.4 mrd to 2.2 mrd. Pole density values of <1.4 mrd are most likely artifacts of the Rietveld analysis with extremely oriented phyllosilicates diffraction peaks overlapping with quartz (Fig. 10). The strongest CPO with a (0001) maximum of 2.3 mrd was observed in Sa1 (with a weak phyllosilicate texture and equiaxed quartz grains) but the pole figure does not correspond to any typical textures documented in quartzites where quartz (0001) CPO generally exceeds 5 mrd, with regular patterns (e.g. Menegon et al., 2008; Toy et al., 2008; Wenk et al., 2019).

We have explored orientation patterns of some accessories. Albite does not display any coherent orientation. Prismatic apatite in Fo3 aligns with (0001) preferentially in the lineation direction X (Fig. 15a), which is comparable with SEM microstructures (Fig. 8b). Biotite in Sa1 displays a weak preferred orientation of (001) (3.1 mrd) at high angles to the foliation plane (Z-axis) (Fig. 15b).

5. Elastic anisotropy based on crystallographic and shape preferred orientation

Elastic properties of rocks are needed to examine seismic velocities and particularly their anisotropy. Slates, composed of elastically highly anisotropic white mica (muscovite) and chlorite with strong alignment are significant contributors to seismic anisotropy in the crust (e.g. Guo et al., 2014; Cárdenes et al., 2021). These slate samples with extraordinary preferred orientation also provide an excellent case to explore the influence of mineral composition, crystallographic and shape preferred orientation on seismic anisotropy and elastic properties of polymineralic rocks. While there are many data on the anisotropy of shales (e.g. Hornby, 1998), there is very little information about slates which are an important component of the continental crust in many orogenic belts (e.g. Christensen and Mooney, 1965; Godfrey et al., 2000). We start with a brief survey on how crystallographic and shape preferred orientation can be used to calculate elastic properties.

Linear elastic properties of a material are described with the twice-symmetric fourth-rank stiffness tensor C_{ijkl} (or compliance S_{ijkl}, which satisfies the "inversion relation" $C_{ijkl} \equiv S^{-1}_{ijkl}$) that, in the general case, has 21 independent components (e.g., Nye, 1985). If single crystal elastic properties ${}^0C$ or ${}^0S$ are known, elastic properties of a textured polycrystal can be estimated by averaging over the 3D ODF. In the simplest form this

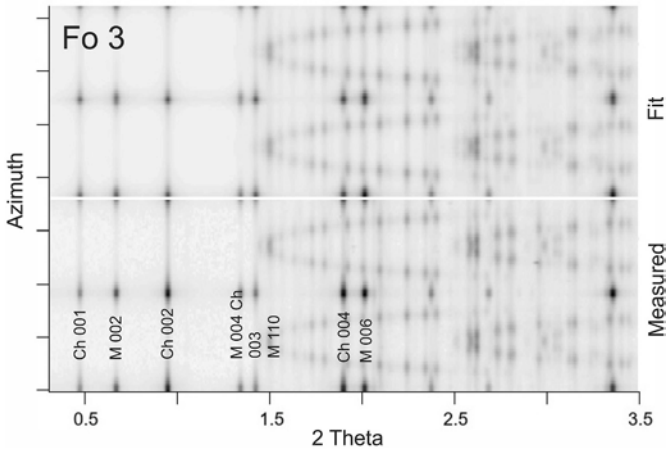

Fig. 11. "Unrolled" diffraction image of Fo3 (Fig. 10a) in MAUD, plotting azimuthal intensities as function of 2-Θ. This corresponds to a stack of 72 integrated diffraction patterns. Some diffraction peaks are indexed (Ch: chlorite, M: muscovite/white mica). Bottom are experimental data and above it the Rietveld fit.

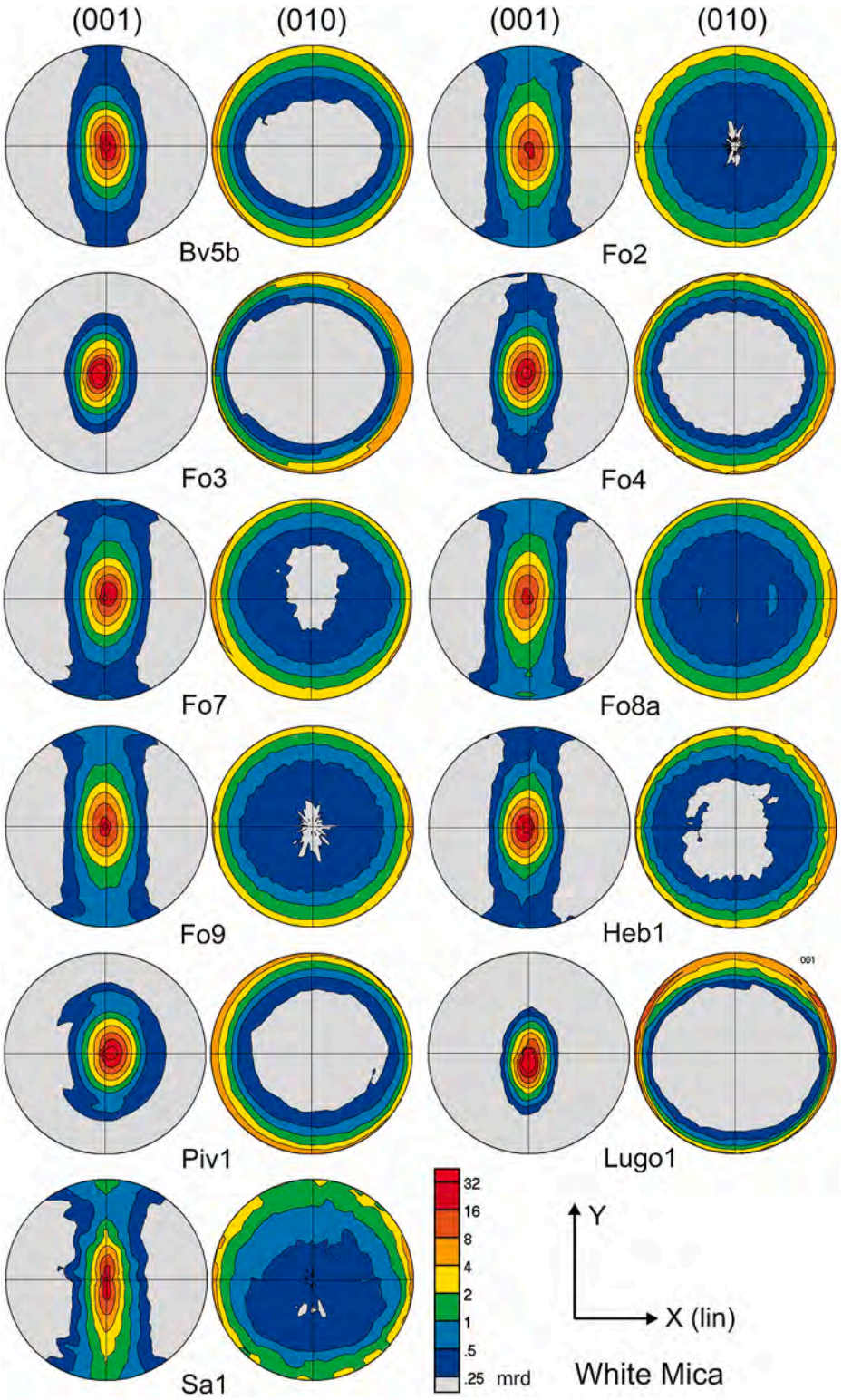

Fig. 12. Pole figures of white mica (muscovite). Equal area projection on cleavage plane. Contours in multiples of random distribution (mrd), logarithmic scale. Coordinates X (lineation) and Y are indicated.

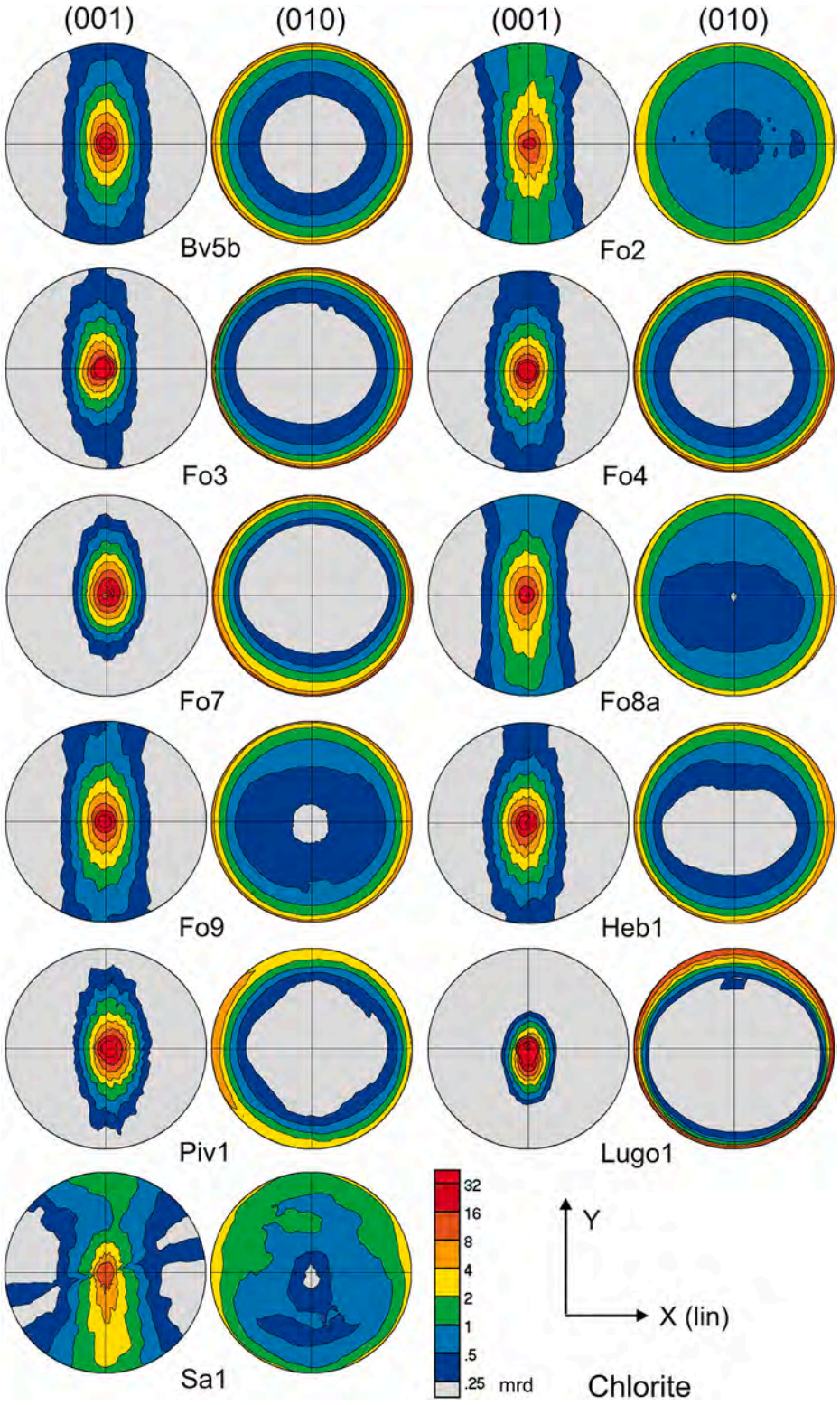

Fig. 13. Pole figures of chlorite. Equal area projection on cleavage plane. Contours in multiples of random distribution, logarithmic scale. Coordinates X (lineation) and Y are indicated.

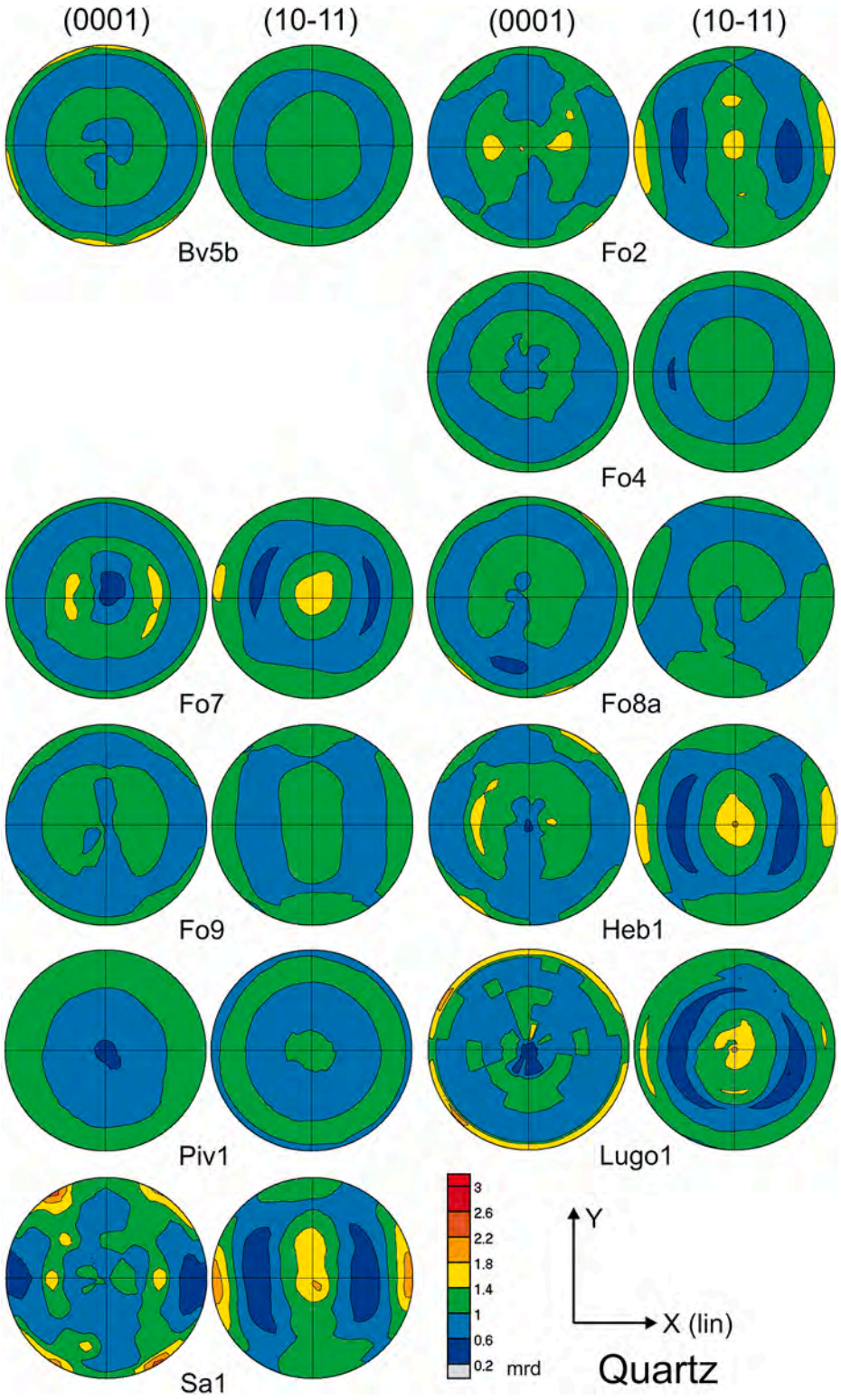

Fig. 14. Pole figures of quartz. Equal area projection on cleavage plane. Contours in multiples of random distribution, linear scale. Coordinates X (lineation) and Y are indicated.

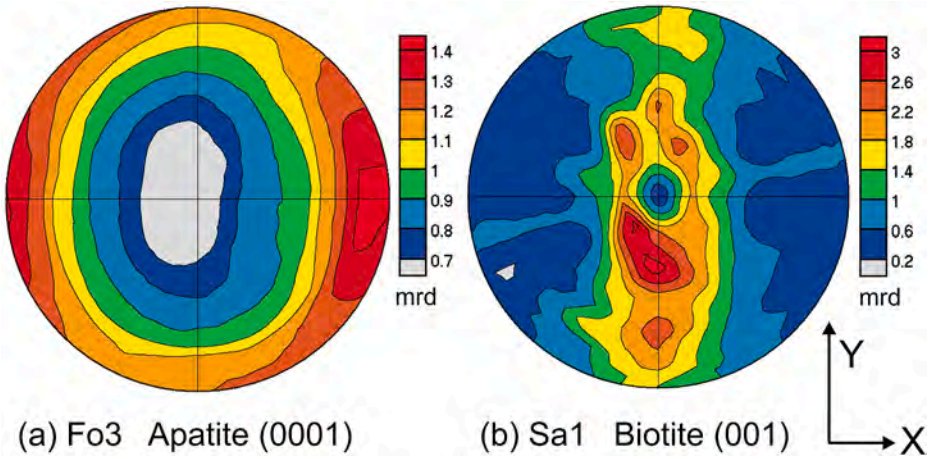

Fig. 15. Pole figures of (a) apatite in Fo3 and (b) biotite in Sa1. Equal area projection on cleavage plane. Contours in multiples of random distribution, linear scale.

Table 3
Preferred orientations of minerals in different samples: 001 pole figure maxima and minima, ODF maximum (in multiples of random distribution, mrd) and for white mica and chlorite angular half-width of the 001 texture maximum in XZ (a) and YZ (b) planes at 1 mrd (boundary between blue and green, in degrees).

Sample	White Mica				Chlorite				Quartz	
	Min 001	Max 001	ODF max	(001) a-b	Min 001	Max 001	ODF max	(001) a-b	Min 001	Max 001
Bv5b	0.1	56.4	94	21–40	0.1	57.0	354	22–50	0.61	1.51
Fo2	0.1	25.2	71	24–52	0.1	21.6	79	23->90	0.41	1.68
Fo3	0.0	69.4	205	20–33	0.1	99.3	503	19–35	–	–
Fo4	0.0	83.5	213	22–36	0.0	83.7	531	21–41	0.43	1.35
Fo7	0.1	38.0	83	24–43	0.0	36.6	660	22–38	0.38	1.70
Fo8a	0.0	29.3	70	22–55	0.0	37.4	143	22–65	0.51	1.43
Fo8b	0.0	36.6	106	22–50	0.0	51.0	132	21–54	0.38	1.54
Fo9	0.0	43.1	138	23–51	0.0	65.1	140	23–50	0.62	1.36
Heb1	0.0	61.8	184	22–51	0.0	44.4	173	22–45	0.35	1.80
Lugo1	0.0	119.8	310	17–32	0.0	125.1	951	16–29	0.15	1.70
Piv1	0.0	46.7	114	24–33	0.0	57.4	461	22–42	0.52	1.32
Sa1	0.0	41.6	139	18–90	0.1	13.5	88	21->90	0.31	2.23

can be done as an arithmetic average of stiffness over all crystals (Voigt average, Voigt, 1887) or an average of compliance (Reuss average, Reuss, 1929). Both averages allow for calculation of properties of multiphase polycrystals by including volume fractions of different phases. A Voigt average is higher (upper bound of the polycrystal properties) than the Reuss average (lower bound). The real elastic properties of the polycrystal are between the two. Different methods were proposed to narrow these bounds, e.g., using an arithmetic mean of Voigt and Reuss results (Hill, 1952), or geometric mean models (Matthies and Humbert, 1995). The latter additionally obey the statistically important group principle (Matthies et al., 2001).

Such relatively simple methods consider only ODFs, volume fractions and single crystal elastic properties of constituent phases, and disregard details of grain interactions, or grain shapes. This could be addressed with finite element methods, but these are rarely applied to such complex anisotropic and heterogeneous materials as multiphase rocks and are mostly limited to studies of isotropic materials or 2D cases (e.g., Makarynska et al., 2008; Zhong et al., 2014; Srisutthiyakorn et al., 2018).

Another approach is to use an iterative self-consistent algorithm that

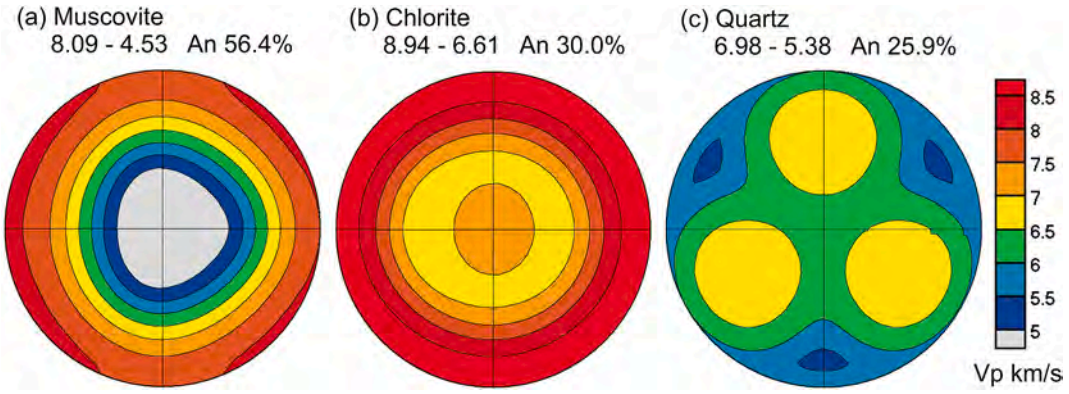

Fig. 16. P-wave velocity distributions of white mica (muscovite), chlorite (projected on cleavage plane (001)) and quartz (with c-axis in center) single crystals. Linear scale. Equal area projection. Minimum and maximum velocity values (in km/s) and anisotropy coefficients An are given.

Table 4
Elastic properties of slates obtained by GMS averaging, expressed as 21 stiffness coefficients (C_{ij} in GPa); P-wave velocity maxima and minima and shear wave splitting (P and dS velocities are in km/s); P-wave anisotropy coefficient An(%); and density (g/cm^3). X is lineation, Z is normal to cleavage. Grain shapes 1:1:0.1 were assumed for phyllosilicates and 1:1:0.2 for quartz.

density	Bv5b	Fo2	Fo3	Fo4	Fo7	Fo8a	Fo9	Heb1	Lugo1	Piv1	Sa1
	2.706	2.693	2.730	2.696	2.716	2.686	2.692	2.684	2.714	2.700	2.701
C_{11}	141.20	135.02	171.54	144.95	134.58	135.80	139.01	142.09	139.79	142.72	131.68
C_{22}	130.40	119.86	159.95	134.97	124.01	119.67	124.50	131.15	134.28	136.9	112.75
C_{33}	83.54	89.06	77.49	83.76	82.43	90.35	88.29	86.72	78.55	82.17	89.26
C_{44}	30.16	33.23	24.06	29.30	30.66	33.23	31.82	30.84	29.30	29.31	34.04
C_{55}	29.84	33.90	23.94	29.28	30.90	33.70	32.12	30.94	28.74	29.23	35.38
C_{66}	51.89	47.93	59.93	53.65	50.39	48.31	49.74	52.29	54.96	54.05	45.82
C_{12}	30.72	28.76	44.58	31.38	27.64	28.25	29.88	30.74	26.70	30.99	26.38
C_{13}	23.23	24.67	28.77	22.76	21.75	23.31	23.88	23.35	18.72	22.97	23.82
C_{14}	0.07	0.12	0.08	−0.03	−0.25	−0.05	−0.01	0.11	0.75	0.04	0.57
C_{15}	−1.42	−1.07	7.08	0.88	−2.73	1.74	0.38	2.21	−0.69	−5.82	−1.20
C_{16}	0.20	−0.39	−0.57	−0.27	−0.31	−0.37	−0.01	−0.29	−0.06	−0.03	−0.09
C_{23}	25.22	26.64	29.87	24.32	23.26	25.82	26.03	25.08	20.23	23.99	25.82
C_{24}	0.49	0.95	0.71	−0.06	−2.21	−0.04	0.03	0.78	5.95	0.02	2.58
C_{25}	−0.17	−0.13	1.09	0.11	−0.24	0.10	0.01	0.25	−0.08	−0.71	0.08
C_{26}	0.09	0.15	−0.49	−0.24	−0.25	−0.16	0.02	−0.11	0.17	−0.03	0.28
C_{34}	0.29	−0.16	0.01	−0.06	−0.31	0.15	0.06	0.05	0.13	−0.16	1.26
C_{35}	−0.01	0.02	0.11	0.05	−0.16	0.07	−0.03	0.00	−0.10	0.05	−0.22
C_{36}	−0.09	0.01	0.21	0.13	0.14	0.06	−0.02	0.12	−0.16	0.01	−0.05
C_{45}	−0.04	−0.03	0.11	0.05	0.05	−0.03	−0.02	0.06	−0.09	0.00	−0.02
C_{46}	−0.56	−0.44	2.60	0.35	−1.03	0.59	0.10	0.84	−0.31	−2.30	−0.27
C_{56}	0.31	0.37	0.26	−0.06	−1.08	0.02	0.04	0.41	2.58	−0.02	1.91
VPmax	6.86	7.08	7.93	7.33	6.72	7.11	7.18	7.27	7.18	7.29	6.98
VPmin	5.27	5.75	5.32	5.56	5.48	5.79	5.72	5.68	5.37	5.51	5.72
An%	26.2	20.7	39.4	27.5	20.3	20.5	22.6	24.6	31.4	27.8	19.8
dS max	1.02	0.75	1.77	1.19	0.73	0.77	0.90	1.05	1.28	1.22	0.63

Table 5
Different models of elastic properties of Lugo1 slate expressed as 21 C_{ij} stiffness coefficients (in GPa); P-wave velocity maxima and minima and shear wave splitting (P and dS velocities are in km/s); P-wave anisotropy coefficient An(%); and density (g/cm^3). Coordinates X is lineation, Z is normal to cleavage. All Lugo1 columns assume measured phyllosilicate and quartz CODs, except column 7 with random quartz COD. Comparison with Tambo gneiss (Vasin et al., 2017), Outokumpu gneiss (Wenk et al., 2012) and Kimmeridge shale (Vasin et al., 2013).

density	Lugo1 slate							Tambo	Outo.	Kimm.
	2.7144							2.660	2.750	2.648
	Voigt	Reuss	GMS	GMS	GMS	GMS	GMS			
Phyllosilicate aspect ratio			1:1:0.01	1:1:0.1	1:1:1	1:1:0.1	1:1:0.1			
Quartz COD							random			
Quartz aspect ratio			1:1:0.2	1:1:0.2	1:1:0.2	1:1:1	1:1:1			
C_{11}	149.1	125.4	140.5	139.8	137.7	139.6	140.6	102.1	105.5	59.0
C_{22}	145.7	119.8	134.5	134.3	133.2	134.1	134.4	90.2	95.4	59.0
C_{33}	88.0	75.7	78.3	78.6	81	78.7	80.2	103.9	78.1	38.1
C_{44}	34.8	26.2	28.8	29.3	30.2	29.3	29.0	33.9	31.8	12.5
C_{55}	34.5	25.7	28.2	28.7	29.7	28.8	28.1	38.3	31.3	12.5
C_{66}	58.5	50.7	54.8	55.0	55.0	54.8	55.0	33.8	39.2	18.8
C_{12}	30.0	20.7	27.4	26.7	25.1	26.7	27.0	25.3	21.5	21.5
C_{13}	18.9	17.2	19.1	18.7	18.0	18.7	17.6	26.8	19.4	20.4
C_{14}	1.0	0.3	0.8	0.7	0.7	0.7	0.9	0.0	−0.9	0
C_{15}	−0.6	−0.6	−0.7	−0.7	−0.6	−0.7	−0.9	0.7	1.1	0
C_{16}	0.0	−0.1	−0.1	−0.1	0.0	−0.1	0.0	0.8	0.9	0
C_{23}	20.0	18.9	20.8	20.2	19.3	20.2	19.7	25.2	21.7	20.4
C_{24}	5.9	5.3	6	5.9	5.7	6.0	6.0	0.4	−0.6	0
C_{25}	−0.1	0.0	−0.1	−0.1	−0.1	−0.1	−0.1	0.0	−0.6	0
C_{26}	0.2	0.2	0.2	0.2	0.2	0.2	0.0	0.1	0.7	0
C_{34}	0.4	−0.4	0.1	0.1	0.0	0.1	−0.1	1.1	−1.4	0
C_{35}	−0.2	0.0	−0.1	−0.1	−0.1	−0.1	0.1	0.5	0.3	0
C_{36}	−0.2	−0.1	−0.1	−0.2	−0.2	−0.2	0.0	0.0	0.0	0
C_{45}	−0.2	−0.1	−0.1	−0.1	−0.1	−0.1	0.0	0.3	0.5	0
C_{46}	−0.3	−0.3	−0.3	−0.3	−0.3	−0.3	−0.3	0.2	−0.3	0
C_{56}	2.3	2.5	2.6	2.6	2.4	2.6	2.8	0.3	−3.3	0
VP max	7.41	6.79	7.20	7.18	7.12	7.17	7.20	6.36	6.23	4.60
VP min	5.56	5.24	5.37	5.37	5.44	5.37	5.41	5.90	5.30	3.69
An%	28.5	25.8	29.1	28.8	26.8	28.7	28.4	7.5	16.1	22.0
dS max	1.11	1.28	1.30	1.28	1.22	1.26	1.31	0.25	0.53	0.48

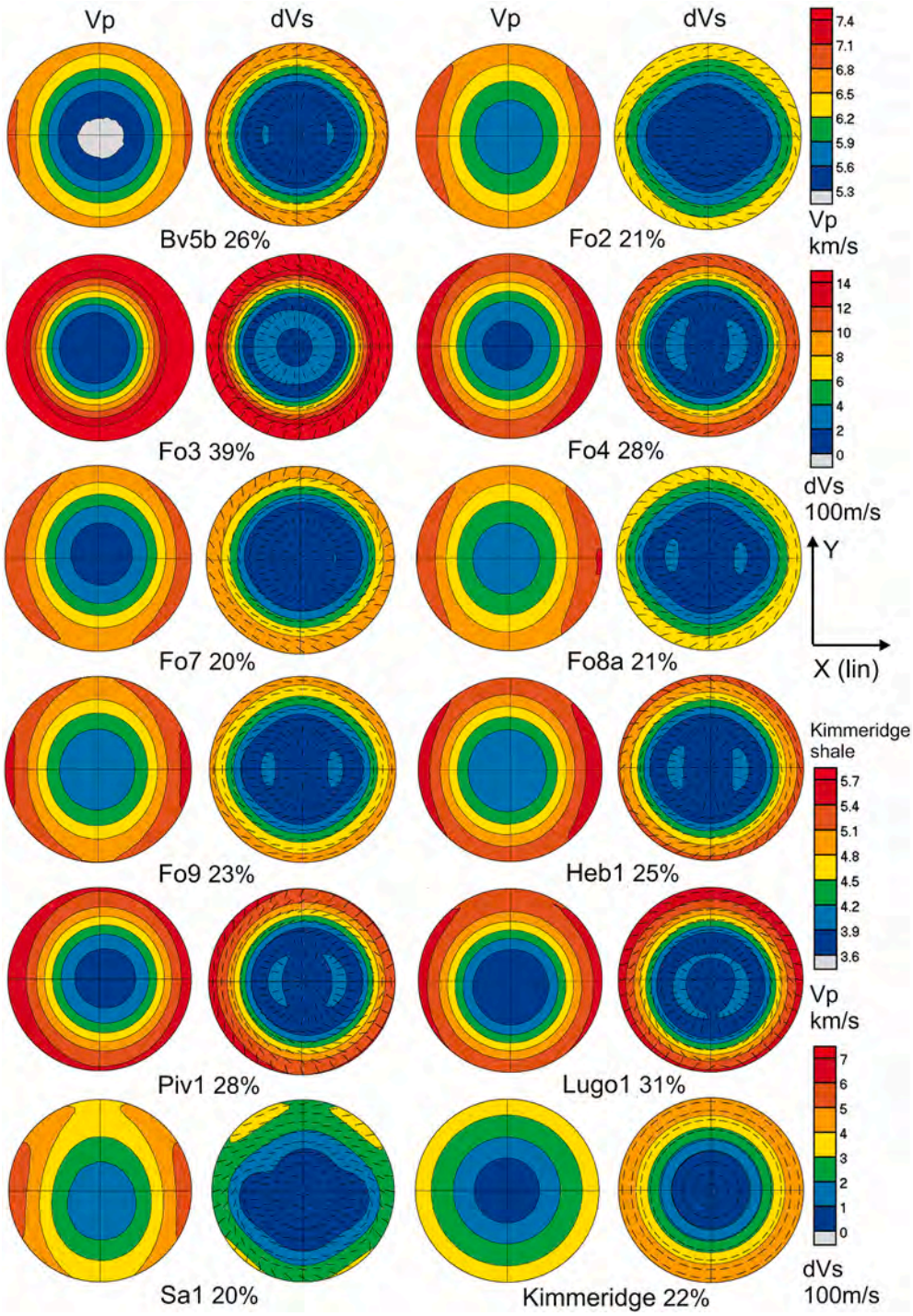

Fig. 17. P and dS velocities as function of direction, equal area projection on the cleavage plane. The first 10 samples are Spanish slates and Sa1 a phyllite. The last one is Kimmeridge shale from the North Sea for comparison and with different intensity scale (from Vasin et al., 2013). For dVs lines indicate polarization of the fast s-wave. Anisotropy coefficient values (%) are given. Coordinates X (lineation) and Y are indicated.

calculates elastic properties of the polycrystal, treating it as an effective medium composed of grains approximated by ellipsoidal inclusions (e.g., Kröner, 1958; Morris, 1970, Fig. 6). To model bulk elastic coefficients of slates we use a modified self-consistent method GeoMIXself (GMS) (Matthies, 2010, 2012) that adds elements of the geometric mean model (Matthies and Humbert, 1995) to conventional self-consistent routines to produce a unique solution for elastic properties exactly obeying the inversion relation. As an effective medium approach, GMS neglects correlations in positions of grains, and thus requires only 'global' orientation distributions. ODFs are obtained from the diffraction experiments described above. Shape orientation distributions (SPO) may be either derived from CPOs considering additional rotations when the grain shape is related to crystallographic cleavage planes as in phyllosilicates (Vasin et al., 2013), or be represented as δ-function in the sample coordinate system if grain shapes are defined by a macroscopic deformation process, as in case of highly flattened quartz grain shapes in the studied slates.

Volume fractions of minerals are available from the Rietveld refinement (Table 2), and single crystal elastic constants of minerals are taken from the literature (Table S6). We use elastic tensors measured by

Vaughan and Guggenheim (1986) for white mica/muscovite (the latter has to be changed to first monoclinic setting to comply with the CPO analysis) and by Heyliger et al. (2003) for quartz. The stiffness tensor of chlorite has been estimated by measurements (Alexandrov and Ryzhova, 1961) and more recently by first principles calculations (Mookherjee and Mainprice, 2014; Ulian et al., 2018). Here we use results from Mookherjee and Mainprice (2014) assuming a monoclinic unit cell. In slates, triclinic chlorite is present but two lattice angles are close to right angles; thus for calculations we used the monoclinic tensor taking into account that it is provided in a coordinate system related to stacking crystal planes and therefore to the grain shape. The first principle calculations are made for clinochlore, a pure Mg-chlorite, while chlorites in slates have a Fe/Mg ratio of ~2 which could affect elastic properties.

Let us demonstrate first the single crystal elastic anisotropies of the three mineral phases that compose most of the slates. Using mineral stiffnesses and densities, elastic wave velocities have been calculated with BEARTEX (Wenk et al., 1998). Fig. 16 displays longitudinal P-velocity distributions, projected on the (001) plane for white mica/-muscovite and chlorite, and on the (0001) plane for quartz. Elastic anisotropy (An) can be qualitatively described using V_P values as An% = $200(V_{Pmax}-V_{Pmin})/(V_{Pmax} + V_{Pmin})$. Clearly white mica/muscovite has the highest elastic anisotropy (56.4%). Chlorite has a much weaker anisotropy (30.0%). Anisotropy of quartz is even weaker (25.9%).

Aspect ratios of mineral grains in slates were assessed from SEM images (Fig. 7, Table 2). Here we use for all samples average {1:1:0.1} grain shapes for phyllosilicates and {1:1:0.2} shapes for quartz (Table 4). Grain shapes of phyllosilicates are linked to their crystal orientation, those of quartz to the sample coordinates (X/Z).

To investigate the effect of the grain shape on slate elastic properties, we used GMS to model Lugo1 slate elasticity assuming different phyllosilicate shapes {X:Y:Z}: {1:1:0.01}, {1:1:0.1} and {1:1:1}, and quartz shapes {1:1:0.1} and {1:1:1} (Table 5). We also explored the effect of quartz assuming {1:1:0.1} for phyllosilicates but having random CPO for quartz with a (1:1:0.2) grain shape and actual CPO for quartz but isotropic shape (1:1:1).

Results for the slate elastic properties are expressed with 21 stiffness coefficients for each slate sample (Table 4) and for different assumptions in the case of Lugo1 (Table 5). C_{11} coefficients, corresponding to the lineation direction X, range from 132 to 172 GPa. C_{33} coefficients, the stiffness along the softest direction Z perpendicular to the cleavage range from 77 to 90 GPa. These stiffness coefficients and slate densities computed from mineral densities and refined volume fractions, were then used to calculate elastic wave velocities with BEARTEX. Distributions of P-wave velocities and shear wave splitting (difference between fast and slow shear wave velocities) in slates are shown in Fig. 17. In all slates, slowest P-waves are perpendicular to the cleavage plane (Z), corresponding to the preferred orientation of (001) normals of phyllosilicates. Highest shear wave splitting is in the XY plane. Dark lines in the shear wave splitting plots indicated the orientation of the fast s-wave.

6. Discussion

6.1. Crystallographic and shape preferred orientation

Preferred orientation patterns for white mica (muscovite) and chlorite in Spanish slates are similar to those observed in a worldwide survey (Wenk et al., 2020). However, Spanish slates consistently display a girdle-like (001) phyllosilicate distribution in pole figures (Figs. 12 and 13). This can be quantified by looking in (001) pole figures at the angular half-width at 1 mrd pole density in the XZ plane and the YZ plane (Table 3). For white mica, the sharpest width in XZ (a) is 17° for Lugo1 and ranges from 17° to 24°. In the YZ plane (b) the range is much broader, from 32° (Lugo1) to 55° (Fo8a). Fo8 is the sample with the macroscopically well-visible inclined bedding plane (Fig. 3b). The difference in width in XZ and YZ is smallest for Piv1 (9°) with an almost axially symmetric pattern. Similar patterns are observed for chlorite. To

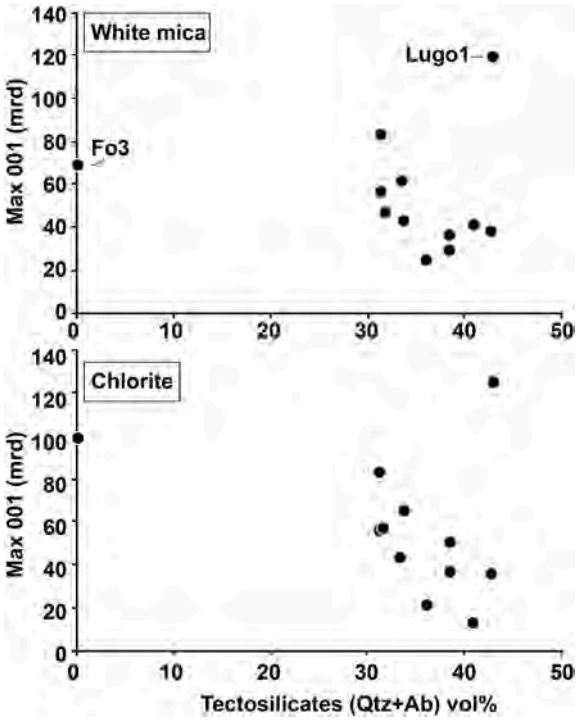

Fig. 18. Comparison of white mica and chlorite CPOs, represented by maximum values of 001 pole figures (mrd) and tectosilicate content (quartz + albite) vol%, of Fo samples, calculated from data in Table 2. Lugo1 and Sa1 are plotted for comparison.

quantify this girdle distribution, it is crucial to project pole figures along Z on the cleavage plane (XY) to avoid distortions due to spherical projections. For projections along the lineation (X) (001) pole figures of phyllosilicates look highly distorted, even for axial symmetry (e.g. Cárdenes et al., 2021).

The girdle distribution observed in Spanish slates is different from some (001) pole figures observed in the Belgian Ardennes (Be-E1, E2), Hunsrück-Germany (Sturtz), Brittany-France (Sin2), and the Eastern Sierra Nevada in California (NS3), which are basically axially symmetric (Fig. 19 in Wenk et al., 2020). Samples described here were subjected not only to axial compression but also plane strain, with extension and simple shear in the lineation direction, as demonstrated by the YZ girdle for white mica and chlorite (001). This is consistent with the structural evolution in this part of the Variscan orogen (Pérez-Estaún et al., 1991; Azor et al., 2019). The sample with the most pronounced crenulation cleavage Sa1 displays the largest YZ spreading of phyllosilicate (001) normals, consistent with the layered microstructure attributed to different deformation episodes with microlithon and cleavage domains (Fig. 8g–i).

Microstructures with fairly euhedral platy crystals of white mica and chlorite, with not much evidence of kinking (e.g. in Fo9, Fig. 8d) or grain boundary sliding, are consistent with recrystallization under stress (Kamb, 1959; Paterson, 1973; Shimizu, 2001), rather than rigid particle rotations that have been proposed by Oertel and Curtis (1972), Oertel (1983) and Sintubin (1994), using the Jeffery (1923) and March (1932) theories. The dominant mechanism appears to be pressure solution and reprecipitation (e.g. Weyl, 1959; Plessmann, 1964, 1966; Durney, 1972; Rutter, 1976; De Boer, 1977; Wright and Platt, 1982; Lee et al., 1986; Ishii, 1988; Kanagawa, 1991; Karasawa and Kano, 1992; Heidelbach et al., 2000; Ho et al., 2001; Imon et al., 2004) and would also account for flat quartz grains growing parallel to phyllosilicate platelets in pressure shadows (e.g. Pabst, 1931; Passchier and Trouw, 2005), with random crystal preferred orientation.

Fo8a has a pronounced bedding plane at 20° to the cleavage (S1)

plane (Fig. 3b), but this does not seem to be expressed significantly in the texture. The bedding plane/cleavage intersection is visible by weak diagonal structures on slaty cleavage surfaces (top left/bottom right in Fig. 4b and c). While the bedding plane is recognized in some hand specimen due to slight compositional variations (Fig. 3b), it is not well expressed in SEM microstructures, except a weak diagonal stacking of platelets top right/bottom left e.g. in Fo8a (Fig. 7f), Piv1 (Fig. 7i) and Lugo1 (Fig. 7j).

One question is the total strain to which slates were subjected. There are no clear passive markers in our samples to account for strain quantification. The development of a penetrative slaty cleavage has been typically related to >50% shortening perpendicular to cleavage plane (e.g. Wood, 1974). A combination of different processes is involved in the development of slaty cleavage. Rigid rotation and intracrystalline plasticity of micas combine with solution-transfer creep in both phyllosilicates and quartz. The observation of strong quartz SPO without CPO points to a dissolution and reprecipitation mechanism, which, under significant stress at low temperature, can generate strong fabrics without significant plastic deformation by dislocation glide (e.g. Czertowicz et al., 2019).

The influence of metamorphic grade on slate microstructures has been discussed (e.g. Siddans, 1972; Wood et al., 1976; Knipe, 1979, 1981; Morris, 1981; Lee et al., 1986; Ho et al., 1995; van Norden et al., 2007; Jacques et al., 2014). In the case of Spanish metasediments studied here, metamorphic grade ranges from lower to upper greenschist facies. Highest grade, with some biotite, applies to Sa1 and Lugo1. In all samples microstructures indicate that white mica and chlorite crystallized in equilibrium with euhedral crystals, only rarely bent and particularly often interlayered at micron-scale (Figs. 7i and 8a, e). It suggests equilibrium growth during the illite/smectite white mica/-chlorite transformation.

The mineral composition is similar in all samples, with white mica, Fe–Mg chlorite and quartz as the main phases, and minor components like albite (<10%, Table 2), depicting an overall textural equilibrium under greenschist facies conditions. Typical lepidoblastic microstructure dominate the fabric, which can be easily correlated to regional axial plane foliation in all cases. Only in the case of the highest metamorphic grade (phyllite Sa1), with the presence of biotite and a crenulation cleavage (e.g. Cosgrove, 1976; Gray, 1977; Gray and Durney, 1979; Passchier and Trouw, 2005), there is a relatively complex evolution (Fig. 8g–i). In Sa1, biotite crystals are large but scarce (<5%) and show a syn/late-kinematic character with respect to the principal foliation (S3 cleavage). Also, Sa1 is the only sample where quartz does not have a flattened grain shape as a result of the formation process of layered microlithons domains (Fig. 8h) and displays significant CPO (Fig. 14). From the white mica (001) YX girdle (Fig. 12) it can be inferred that the sample experienced more or less asymmetric expension rather than plane strain.

Determining lattice parameters of phyllosilicates in the Rietveld refinement (Supplementary Tables S3 and S5), as well as estimating chemical composition with EDS analyses (Supplementary Tables S2 and S4) suggests no systematic variations with metamorphic grade. Chlorites have all similar high Fe/Mg ratios (~1.6), perhaps slightly lower for high grade Lugo1 and Sa1 (~1.3).

There are consistent accessories (<3%) in most samples: apatite, pyrite and rutile (Table 2). Apatite with prismatic shape deformed with phyllosilicates and developed significant texture with [0001] aligned in the lineation direction (X in Fig. 15a). Monazite has been documented in Fo3, Fo8 and Fo9. Lugo1 contains relatively large phenocrysts of ilmenite (Fig. 8f) that grew and replaced phyllosilicates and quartz. Albite is present in many samples (0–10%, Table 2) but displays no significant preferred orientation.

One of the most important properties of slates related to microstructures is fissility (Cárdenes et al., 2014). Splitting into thin slate plates (i.e. 3-10 mm thickness) up to certain dimensions (minimum 32 × 20 cm) is critical to determine the potential of the rock for being a high-quality roofing slate (Fig. 4, e.g. García-Guinea et al., 1998). There is a close correlation between mechanical properties of slates and their fabric (i.e. bending strength; Wagner, 2007; Gómez-Fernández et al., 2012). The quartz content is a significant factor modifying both fabric and mechanical response of the slate, affecting its workability and slate hardness (Cárdenes et al., 2014).

In our samples quartz shows a strong shape preferred orientation (Fig. 7), but an almost random texture (Fig. 14). There appears to be a slight tendency for a concentration of poles of positive rhombs (101) perpendicular to the cleavage plane, which could be attributed to mechanical Dauphiné twinning (e.g. Minor et al., 2018). But this is questionable because the strong quartz (101 + 011) diffraction peak overlies with the strong white mica (006) peak (Fig. 10b).

To explore the interlink between mineral composition and phyllosilicates texture, we have represented in Fig. 18 the covariance of the (001) pole figure maximum value (mrd) of white mica and chlorite, and the abundance of tectosilicates in the rock (quartz + albite, Table 2). Our results show that in most samples within the common compositional range for Spanish roofing slates, phyllosilicate texture strength decreases as tectosilicate content increases (Fig. 18). Both white mica and chlorite display a similar behavior as suggested by microstructural observations (Figs. 7 and 8). Even slates like Fo3, with a very low content of tectosilicates, are compatible with this trend.

6.2. Elastic anisotropy

All slates have strong elastic anisotropy as expressed by P- and S-wave velocities calculated based on microstructures and preferred orientation (Table 4, Fig. 17). There is a P-wave velocity minimum perpendicular to the cleavage (in Z direction) and a maximum in the lineation direction (X) with strong shear-wave splitting in the cleavage plane. The P-wave anisotropy coefficient An ranges from 19.8% (Sa1) to 39.4% (Fo3). Fo3 is the sample without quartz, almost entirely composed of phyllosilicates. Maximum shear wave splitting in the 11 samples ranges from 0.6 to 1.8 km/s. Fo3 demonstrates maximum splitting due to minimal quartz content.

The Spanish slates provide excellent samples to explore the assumptions of different averaging models and particularly the influence of grain shape on anisotropy in a polymineralic rock. They are highlighted in Table 5 for Lugo1. As was mentioned earlier, the Voigt model provides an upper bound for polycrystal elastic properties with high P-wave velocities, while the Reuss model provides a lower bound with lower velocities, the GMS model provides intermediate results. There is not much difference between extremely flat grains of phyllosilicates (1:1:0.01) and flat grains corresponding best with observed microstructures (1:1:0.1). Both models provide high P-wave anisotropy (An) and shear wave splitting values (dS max) (Table 5). Assuming spherical phyllosilicate grains (1:1:1) results in a 5% lower An, as well as lower shear wave splitting. Thus, the sophisticated GMS model improves estimates of elastic anisotropy. Considering random CPO or spherical grain shapes for quartz instead of oriented {1:1:0.2} platelets barely affects slate elastic properties and anisotropy.

Rather low An values of ≈13.6 ± 3.0% were recently reported for some Spanish slates investigated with EBSD and explored for elastic anisotropy with the Hill model (Cárdenes et al., 2021), compared to our results with An 20–40%, Table 5). This could be attributed both to underestimation of phyllosilicate content with EBSD and the simplified arithmetic mean of the Hill approach, which disregards grain shapes.

In Table 5 we also compare elastic anisotropy of Lugo1 slate with gneiss and shale. For amphibolite facies Tambo muscovite gneiss modeled and measured elastic properties show much lower anisotropy than slate (Vasin et al., 2017) with only 7.5% anisotropy compared with ~28% for slate. This is largely due to the much lower phyllosilicate content (17% muscovite) and lower CPO (10 mrd). For biotite gneiss from the Outokumpu drill hole in Finland with 23% biotite and 22 mrd, anisotropy is 16% (Kern et al., 2009; Wenk et al., 2012). This is similar to

other studies of gneiss and schists (e.g. Godfrey et al., 2000; Kern et al., 2001; Cholach and Schmitt, 2006; Valcke et al., 2006; Wenk et al., 2010; Fazio et al., 2017).

Anisotropy is also stronger in the slates studied here than in shales, even after taking aligned porosity into account, e.g. Kimmeridge shale (Hornby, 1998; Vernik and Liu, 1997; Vasin et al., 2013, Table 5), Mont Terri clay (Wenk et al., 2008), Posidonia shale (Kanitpanyacharoen et al., 2012) and experimentally compressed clay mixtures (Voltolini et al., 2009). For Kimmeridge shale with 67% phyllosilicates and illite (001) at 6.7 mrd, anisotropy is 22%, including aligned porosity (Vasin et al., 2013).

For slates we did not take microfractures into account for calculating elastic properties. Some are revealed by black regions in SEM images (Figs. 5 and 7). They do not seem associated with the cleavage plane, are rather equiaxed and may have originated during sample preparation. Oriented fractures have been considered in GMS modeling of shales (e.g. Vasin et al., 2013), gneiss (e.g. Vasin et al., 2017) and Westerley granite (Lokajicek et al., 2021).

Shales transforming to slates in metasedimentary basins as in Spain may contribute significantly to observed seismic anisotropy in the crust (e.g. Christensen and Mooney, 1965). In fact, several recent studies document seismic anisotropy in Northern Spain (e.g. Barruol et al., 1998; Díaz et al., 2006; Acevedo et al., 2021), attributing it tentatively to serpentinite, even though anisotropy of slates is much higher and may be very significant for interpreting seismic data. From a regional point of view the Iberian Massif low-grade metasediments show a pervasive tectonic foliation related to the Variscan orogeny deformation in the Paleozoic (Azor et al., 2019). The presence of kilometer-scale volumes of highly anisotropic rocks like slates and phyllites, should be considered to evaluate, for example, the significance on the reflectivity (Blangy, 1994; Godfrey et al., 2000), or the interpretation of the recent observsations in seismic experiments in the Iberian Massif (e.g. Díaz et al., 2006; Ruiz et al., 2017; Palomeras et al., 2021). But keep in mind that the very high anisotropy in hand specimens described in Fig. 17 and Table 4 is modified by folds on the macroscopic scale (Figs. 1c and 2).

6.3. Suggestions for future studies

This study on microstructures, preferred orientation and seismic anisotropy adds important new information on these enigmatic rocks but it also opens new questions that should be addressed in the future. While there is a lot of information on shales and slates, there is little information how a shale transforms to a slate. Material from Northern Spain may provide an opportunity since old shales are available and transformations have been investigated geochemically (e.g. Clauer and Weh, 2014). This transformation should also be investigated experimentally to shed light on the mechanisms of dissolution – reprecipitation at low grade conditions.

Another issue is organic matter. “Organic” slates/shales, or argillites, have been described in coal deposits, but very little is known about the transition of argillites into slates and corresponding microstructures and textures (e.g. Large et al., 1994; Suchy et al., 2007; Suárez-Ruiz et al., 2012). Slates from the California Shoe Fly Ftn. with a high carbon content display only very weak fabrics. The Middle-Upper Ordovician slates sampled in the Rozadais and Luarca Formations have similar organic matter contents (<0.3%), while the Lower Cambrian and Upper Proterozoic phyllites typically show no trace of organic matter (e.g. Cárdenes et al., 2014). As a consequence, the Ordovician slates depict dark black-grey colors, while high-grade slates are greenish-grey. The green color of the Cambrian slate (Lugo1, Fig. 4c) has been attributed to the presence of clinochlore (Cárdenes et al., 2014), although in our samples Lugo1 has a similar fairly high iron content as the other chlorites (Supplementary Table S4). Lugo1 has the strongest preferred orientation, visible in its regular horizontal alignment of phyllosilicate grains (Fig. 7j).

Another point is experimental studies of slate anisotropy at high pressure. This was so far only approached with measurements at ambient conditions, subject to an excessive influence of open fractures, as demonstrated in the recent studies of Guo et al. (2014) and Cárdenes et al. (2021). Experiments with state-of-the-art methods such as Kern et al. (2009) and Lokajicek et al. (2021) would add valuable new information.

7. Conclusions

A study of greenschist-facies metamorphic slates from Northern Spain reveals strong preferred orientation of white mica (muscovite) and chlorite. Fairly euhedral grain shapes suggest formation from original shales by pressure solution and reprecipitation with recrystallization. The high CPO could be quantified with high energy synchrotron X-ray diffraction and Rietveld texture analysis. Results are about an order of magnitude higher than previously documented with conventional methods such as pole figure goniometry. By contrast quartz, a significant percentage of slate compositions, has also flattened shapes, but random CPO. With increasing quartz content phyllosilicate CPO decreases. The girdle-like distribution of white mica and chlorite (001) CPO implies that a significant proportion of strain was plane strain. Due to high CPO of phyllosilicates slates display strong elastic anisotropy (20–40%) and since they are important components in tectonic settings around the world, including our sampling locations in Northern Spain, they strongly contribute to observed seismic anisotropy in the crust, which should be incorporated into future seismic models.

Credit authorship contribution statement

All authors contributed to experiments, data analysis, writing and reviewing the manuscript. Hans-Rudolf Wenk conceptualized the project, collected samples, performed synchrotron experiments at APS. Jingyi Huang performed the Rietveld data analysis to obtain quantitative texture information. Michelle Devoe was in charge of SEM analyses to reveal microstructures. Juan Gomez-Barreiro wrote the section on geologic setting and collected samples. Yang Ren was in charge of synchrotron diffraction experiments at APS. Santos Barrios-Sanchez contributed to the geologic setting. Roman Vasin was in charge of the modeling of elastic properties.

Declaration of competing interest

The authors declare the following financial interests/personal relationships which may be considered as potential competing interests: Hans-Rudolf Wenk reports financial support was provided by University of California Berkeley. Hans-Rudolf Wenk reports a relationship with University of California Berkeley that includes: funding grants.

Data availability

Data will be made available on request.

Acknowledgements

We acknowledged access to beamline 11-ID-C of the Advanced Photon Source at Argonne National Laboratory and supported by DOE Office of Science under Contract No. DE-AC02-06CH11357 and the Zeiss EVO SEM at EPS, UC Berkeley. HRW is appreciative for support from NSF (EAR 2154351 and 2054951) and DOE-BES (DE-FG02-05ER15637) and from The Fulbright Foundation for a fellowship in Salamanca. JH was supported by the China Scholarship Council and National Key Research and Development Program No. 2016YFC0303902-04. JGB appreciates financial support from MCIN/AEI/10.13039/501100011033, PID2020-117332 GB-C21. We greatly acknowledge discussions and access to quarries by Victor Cárdenes (Oviedo University) and José Eladio (SAMACA at Valdeorras). John Grimsich at UC

Berkeley helped with sample preparation and SEM analyses. Crucial for this study were software packages MAUD developed by Luca Lutterotti and GeoMIXSelf developed by Siegfried Matthies. We are grateful for their help. We appreciate comments by Toru Takeshita, Toshiaki Masuda, Ichiko Shimizu and an anonymous reviewer which were of great help for improving the manuscript.

Appendix A. Supplementary data

Supplementary data to this article can be found online at https://doi.org/10.1016/j.jsg.2022.104730.

References

Acevedo, J., Fernandez-Viejo, G., Llana-Funez, S., Lopez-Fernandez, C., Olona, J., 2021. Upper-crustal seismic anisotropy in the Cantabrian Mountains (North Spain) from shear-wave splitting and ambient noise interferometry analysis. Seismol Res. Lett. 92, 421–436.

Alexandrov, K.S., Ryzhova, T.V., 1961. Elastic properties of rock-forming minerals. II. Layered silicates. Bull. Academy Sciences USSR, Geophys. Series 9, 1165–1168.

Antao, S.M., Hassan, I., Wang, J., Lee, P.L., Toby, B.H., 2008. State-of-the-art high resolution powder x-ray diffraction (HRPXRD) illustrated with Rietveld structure refinement of quartz, sodalite, tremolite, and meionite. Can. Mineral. 46, 1501–1509.

Azor, A., Días da Silva, I., Gómez Barreiro, J., González Clavijo, E., Martínez Catalán, J. R., Simancas, J.F., Martínez Poyato, s D., Pérez Cácere, s I., González Lodeiro, F., Expósito, I., Casas, J.M., Clariana, P., García-Sansegundo, J., Margalef, A., 2019. Deformation and structure. In: Quesada, C., Oliveira, T. (Eds.), The Geology of Iberia: A Geodynamic Approach: Volume 2: the Variscan Cycle 307-348. Springer International Publishing, ISBN 978-3-030-10518-1. https://doi.org/10.1007/978-3-030-10519-8.

Barrois, C., 1882. Recherches sur les terrains anciens des Asturies et la Galicie. Soc. Géol. Fr. Mém. 2.

Barruol, G., Souriau, A., Vauchez, A., Díaz, J., Gallart, J., Tubia, J., Cuevas, J., 1998. Lithospheric anisotropy beneath the Pyrenees from shear-wave splitting. J. Geophys. Res. 103, 30,039–30,053.

Barros Lorenzo, J.C., 1989. Nuevos datos geológicos y cartográficos sobre el flanco Sur del Sinclinorio de Truchas. Cadernos do Laboratorio Xeolóxico de Laxe 14, 93–116.

Blangy, J.P., 1994. AVO in transversely isotropic media - an overview. Geophysics 59, 775–781. https://doi.org/10.1190/1.1443635.

Bohlen, S.R., Peacor, D.R., Essene, E.J., 1980. Crystal chemistry of a metamorphic biotite and its significance in water barometry. Am. Mineral. 65, 55–62.

Brocher, T.M., Christensen, N.I., 1990. Seismic anisotropy due to preferred mineral orientation observed in shallow crustal rocks in southern Alaska. Geology 18 (8), 737–740. https://doi.org/10.1130/0091-7613(1990)018<0737:SADTPM>2.3.CO;2.

Caglioti, G., Paoletti, A., Ricci, F.P., 1958. Choice of collimators for a crystal spectrometer for neutron diffraction. Nucl. Instrum. 3, 223–228.

Cárdenes, V., Ponce de León, M., Rodríguez, X.A., Rubio-Ordoñez, A., 2019. Roofing slate industry in Spain: history, geology, and geoheritage. Geoheritage 11 (1), 19–34. https://doi.org/10.1007/s12371-017-0263-y.

Cárdenes, V., Rubio-Ordoñez, A., Monterroso, C., Calleja, L., 2013. Geology and geochemistry of Iberian roofing slates. Chem. Erde 73, 373–382.

Cárdenes, V., Rubio-Ordoñez, A., Wichert, J., Cnudde, J.P., Cnudde, V., 2014. Petrography of roofing slates. Earth Sci. Rev. 138, 435–453.

Cárdenes, V., López-Sánchez, M.A., Barou, F., Olona, J., Llana-Fúnez, S., 2021. Crystallographic preferred orientation, seismic velocity and anisotropy in roofing slates. Tectonophysics 808, 228815. https://doi.org/10.1016/j.tecto.2021.228815.

Chen, C.T., Chan, Y.C., Beyssac, O., Lu, C.Y., Chen, Y.G., Malavieille, J., Kidder, S.B., Sun, H.-C., 2019. Thermal history of the Northern Taiwanese slate belt and implications for wedge growth during the Neogene arc-continent collision. Tectonics 38 (9), 3335–3350.

Cholach, P.Y., Schmitt, D.R., 2006. Intrinsic elasticity of a textured phyllosilicate aggregate: relation to the seismic anisotropy of shales and schists. J. Geophys. Res. 111, B09410 https://doi.org/10.1029/2005JB004158.

Christensen, N.I., Mooney, W.D., 1965. Seismic velocity structure and composition of the continental crust: a global view. J. Geophys. Res. 100, 9761–9788. https://doi.org/10.1029/95JB00259.

Clauer, N., Weh, A., 2014. Time constraints for the tectono-thermal evolution of the Cantabrian Zone in NW Spain by illite K-Ar dating. Tectonophysics 623, 39–51. https://doi.org/10.1016/j.tecto.2014.03.013.

Cosgrove, J.W., 1976. The formation of crenulation cleavage. J. Geol. Soc. 132, 155–178. https://doi.org/10.1144/gsjgs.132.2.0155.

Czertowicz, T.A., Takeshita, T., Arai, S., Yamamoto, T., Ando, J.I., Shigematsu, N., Fujimoto, K.I., 2019. Prog. Earth Planet. Sci. 6, 25. https://doi.org/10.1186/s40645-019-0261-6.

De Boer, R.B., 1977. Pressure solution: theory and experiments. Tectonophysics 39, 287–301. https://doi.org/10.1016/0040-1951(77)90101-9.

Díaz, J., Gallart, J., Ruiz, M., Pulgar, J.A., López, C., González-Cortina, J.M., 2006. Probing seismic anisotropy in North Iberia from shear wave splitting. Phys. Earth Planet. In. 158, 210–225. https://doi.org/10.1016/j.pepi.2005.12.011.

Dieterich, J.H., 1969. Origin of slaty cleavage in folded rocks. Am. J. Sci. 267, 155–165. https://doi.org/10.2475/ajs.267.2.155.

Díez Balda, M.A., Vegas, R., González Lodeiro, F., 1990. Central-iberian zone. Structure. In: Dallmeyer, R.D., Martínez García, E. (Eds.), Pre-Mesozoic Geology of Iberia. Springer, pp. 172–188.

Díez Balda, M.A., Martínez Catalán, J.R., Ayarza Arribas, P., 1995. Syn-collisional extensional collapse parallel to the orogenic trend in a domain of steep tectonics: the Salamanca Detachment Zone (Central Iberian Zone, Spain). J. Struct. Geol. 17, 163–182.

Durney, D.W., 1972. Solution transfer, an important geological deformation mechanism. Nature 235, 315–317. https://doi.org/10.1038/235315a0.

Fazio, E., Punturo, R., Cirrincione, R., Kern, H., Pezzino, A., Wenk, H.-R., Goswami, S., Mamtani, M.A., 2017. Quartz preferred orientation in naturally deformed mylonitic rocks (Montalto Shear Zone - Italy): a comparison of results by different techniques, their advantages and limitations. Int. J. Earth Sciences 106, 2259–2278. https://doi.org/10.1007/s00531-016-1424-y.

García-Guinea, J., Lombardero, M., Roberts, B., Peto, A., 1998. Mineralogy and microstructure of roofing slate: thermo-optical behaviour and fissility. Mater. Construcción 48, 37–48.

García-Guinea, J., Lombardero, M., Roberts, B., Taboada, J., 1997. Spanish roofing slate deposits. Trans. Inst. Min. Metall., Sect. B 106, 205–214.

Godfrey, N.J., Christensen, N.I., Okaya, D.A., 2000. Anisotropy of schists: contribution of crustal anisotropy to active source seismic experiments and shear wave splitting observations. J. Geoph. Res. 105 (B12), 27991–28007. https://doi.org/10.1029/2000JB900286.

Goldstein, A., Knight, J., Kimball, K., 1998. Deformed graptolites, finite strain and volume loss during cleavage formation in rocks of the taconic slate belt, New York and Vermont, USA. J. Struct. Geol. 20, 1769–1782.

Gómez Barreiro, J., Martínez Catalán, J.R., Arenas, R., Castiñeiras, P., Abati, J., Díaz García, F., Wijbrans, J.R., 2007. Tectonic evolution of the upper allochthon of the Órdenes Complex (northwestern Iberian Massif): structural constraints to a polyorogenic peri-Gondwanan terrane. Special paper Geol, Soc, America 423, 315–332.

Gómez Barreiro, J., Catalán, J.R.M., Díez Fernández, R., Arenas, R., Diaz Garcia, F., 2010. Upper crust reworking during gravitational collapse: the Bembibre–Pico Sacro detachment system (NW Iberia). J. Geol. Soc. 167, 769–784.

Gómez-Fernández, F., Castañón, A.M., Ward, C.R., 2012. Analysis of the methodology of the petrographic examination test (European Standard EN 12326-2) and the relation between petrography and modulus of rupture for Spanish roofing slates. Eng. Geol. 141, 114–123.

González Lodeiro, F., Martínez Catalán, J.R., De Pablo Maciá, J.G., Pérez González, A., 1979. Mapa Geológico de España e. 1:50.000, Hoja No. 48 (08-05) (Meira). Instituto Geológico y Minero de España, Madrid.

Gray, D.R., 1977. Some parameters which effect the morphology of crenulation cleavage. J. Geol. 85, 763–780.

Gray, D.R., Durney, D.W., 1979. Crenulation cleavage differentiation: implications of solution-deposition processes. J. Struct. Geol. 1, 73–80. https://doi.org/10.1016/0191-8141(79)90023-3.

Guggenheim, S., Chang, Y.H., Koster van Groos, A.F., 1987. Muscovite dehydroxylation: high temperature studies. Am. Mineral. 72, 537–550.

Guo, B.B., Wang, H.C., Zhao, W.H., Ji, S.C., Sun, D.S., Li, A.W., Long, C.X., 2014. Analysis of seismic anisotropy of the typical slate from the Gaoligong mountains, Yunnan province, China. Chin. J. Geophys. 57, 154–165.

Gutiérrez-Marco, J.C., Robardet, M., Rábano, I., Sarmiento, G.N., San José Lancha, M.A., Herranz Araújo, P., Pieren Pidal, A.P., 2002. Ordovician. In: Gibbons, W., Moreno, T. (Eds.), The Geology of Spain. The Geological Society, London, pp. 31–49.

Gutiérrez-Marco, J.C., Piçarra, J.M., Meireles, C.A., Cózar, P., García-Bellido, D.C., Pereira, Z., Vaz, N., Pereira, S., Lopes, G., Oliveira, J.T., Quesada, C., Zamora, S., Esteve, J., Colmenar, J., Bernárdez, E., Coronado, I., Lorenzo, S., Sá, A.A., Dias da Silva, Í., González-Clavijo, E., Díez-Montes, A., Gómez-Barreiro, J., 2019. Early ordovician–devonian passive margin stage in the gondwanan units of the iberian Massif. In: Quesada, C., Oliveira, T. (Eds.), The Geology of Iberia: A Geodynamic Approach. Springer, pp. 75–98.

Haerinck, T., Wenk, H.-R., Debacker, T., Sintubin, M., 2015. Preferred mineral orientation in a chloritoid-bearing slate in relation to its magnetic fabric. J. Struct. Geol. 71 (2), 125–135.

Heidelbach, F., Post, A., Tullis, J., 2000. Crystallographic preferred orientation in albite samples deformed experimentally by dislocation and solution precipitation creep. J. Struct. Geol. 22, 1649–1661.

Herbosch, A., Liégeois, J.P., Gärtner, A., Hofmann, M., Linnemann, U., 2020. The Stavelot-Venn Massif (Ardenne, Belgium), a rift shoulder basin ripped off the West African craton: cartography, stratigraphy, sedimentology, new U-Pb on zircon ages, geochemistry and Nd isotopes evidence. Earth Sci. Rev. 203, 103142.

Heyliger, P., Ledbetter, H., Kim, S., 2003. Elastic constants of natural quartz. J. Acoustical Soc. America 114, 644–650. https://doi.org/10.1121/1.1593063.

Hill, R., 1952. The elastic behaviour of a crystalline aggregate. Proc. Phys. Soc. 65, 349–354.

Ho, N.-C., Peacor, D.R., van der Pluijm, B.A., 1995. Reorientation mechanisms of phyllosilicates in the mudstone-to-slate transition at Lehigh Gap, Pennsylvania. J. Struct. Geol. 17, 345–356. https://doi.org/10.1016/0191-8141(94)00065-8.

Ho, N.-C., van der Pluijm, B.A., Peacor, D.R., 2001. Static recrystallization and preferred orientation of phyllosilicates: michigamme Formation, northern Michigan, USA. J. Struct. Geol. 23, 887–893. https://doi.org/10.1016/S0191-8141(00)00162-0.

Hornby, B.E., 1998. Experimental laboratory determination of the dynamic elastic properties of wet, drained shales. J. Geophys. Res. 103, 29945–29964. https://doi.org/10.1029/97JB02380.

Hughes, J.M., Cameron, M., Crowley, K.D., 1989. Structural variations in natural F, OH, and Cl apatites. Am. Mineral. 74, 870–876.
Hutchinson, W.B., Nes, E., 1992. Texture development during grain growth – a useful rule-of-thumb. Proc. Grain Growth in Polycrystalline Materials I. Mater. Sci. Forum 94–96, 385–390.
Imon, R., Okudaira, T., Kanagawa, K., 2004. Development of shape and lattice-preferred orientations of amphibole grains during initial cataclastic deformation and subsequent deformation by dissolution-precipitation creep in amphibolites from the Ryoke metamorphic belt, SW Japan. J. Struct. Geol. 26, 793–805.
Ishii, K., 1988. Grain growth and re-orientation of phyllosilicate minerals during the development of slaty cleavage in the South Kitakami Mountains, northeast Japan. J. Struct. Geol. 10, 145–154. https://doi.org/10.1016/0191-8141(88)90112-5.
Jacques, D., Derez, T., Muchez, P., Sintubin, M., 2014. Syn- to late-orogenic quartz veins marking a retrograde deformation path in a slate belt: examples from the High-Ardenne slate belt (Belgium). J. Struct. Geol. 58, 43–58.
Jeffery, G.B., 1923. The motion of ellipsoidal particles immersed in a viscous fluid. Proc. R. Soc. London, A 102, 161–179.
Ji, S.C., Shao, T.B., Michibayashi, K., Oya, S., Satsukawa, T., Wang, Q., Zhao, W.H., Salisbury, M.H., 2015. Magnitude and symmetry of seismic anisotropy in mica- and amphibole-bearing metamorphic rocks and implications for tectonic interpretation of seismic data from the southeast Tibetan Plateau. J. Geophys. Res. Solid Earth 120, 6404–6430.
Julivert, M., Fontboté, J.M., Ribeiro, A., Nabais Conde, L.E., 1972. Mapa Tectónico de la Península Ibérica y Baleares E. 1:1.000.000. Inst. Geol. Min. Esp, Madrid.
Kamb, W.B., 1959. Theory of preferred crystal orientation developed by crystallization under stress. J. Geology 67, 153–170.
Kanagawa, K., 1991. Change in dominant mechanisms for phyllosilicate preferred orientation during cleavage development in the Kitakami slates of NE Japan. J. Struct. Geol. 13 (8), 927–943.
Kanitpanyacharoen, W., Kets, F.B., Wenk, H.-R., Wirth, R., 2012. Preferred orientation, microstructures and porosity analyses of Posidonia shales. Clay Clay Miner. 60, 315–329. https://doi.org/10.1346/CCMN.2012.0600308.
Karasawa, Y., Kano, K., 1992. Formation and deformation process of the slate belt in the Setogawa Group (the Shimanto Belt) of the eastern Akaishi Mountains, easternmost southwest Japan. J. Geol. Soc. Japan 98, 761–777.
Kern, H., Popp, T., Gorbatsevich, F., Zharikow, A., Lobanov, K.V., Smirnov, Y.P., 2001. Pressure and temperature dependence of VP and VS in rocks from the superdeep well and from surface analogues at Kola and the nature of velocity anisotropy. Tectonophysics 338, 113–134.
Kern, H., Mengel, K., Strauss, K.W., Ivankina, T.I., Nikitin, A.N., Kukkonen, I.T., 2009. Elastic wave velocities, chemistry and modal mineralogy of crustal rocks sampled by the Outokumpu scientific drill hole. Phys. Earth Planet. In. 175, 151–166.
Kisch, H.J., 1990. Calibration of the anchizone: a critical comparison of illite 'crystallinity' scales used for definition. J. Metamorph. Geol. 8, 31–46.
Knipe, R.J., 1979. Chemical changes during slaty cleavage development. Bull. Mineral. 102, 206–209.
Knipe, R.J., 1981. The interaction of deformation and metamorphism in slates. Tectonophysics 78, 249–272. https://doi.org/10.1016/0040-1951(81)90016-0.
Knipe, R.J., White, S.H., 1977. Microstructural variation of an axial plane cleavage around a fold. A H.V.E.M. study. Tectonophysics 39, 355–381.
Kröner, E., 1958. Berechnung der elastischen Konstanten des Vielkristalls aus den Konstanten des Einkristalls. Z. Phys. 151, 504–518.
Large, D.J., Christy, A.G., Fallick, A.E., 1994. Poorly crystalline carbonaceous matter in high grade metasediments: implications for graphitisation and metamorphic fluid composition. Contrib. Mineral. Petrog. 116, 108–116.
Lee, J.H., Peacor, D.R., Lewis, D.D., Wintsch, R.P., 1986. Evidence for syntectonic crystallization for the mudstone to slate transition at Lehigh Gap, Pennsylvania, USA. J. Struct. Geol. 8, 767–780. https://doi.org/10.1016/0191-8141(86)90024-6.
Lokajicek, T., Vasin, R., Svitek, T., Petruzalek, M., Kotrly, M., Turkova, I., Onysko, R., Wenk, H.-R., 2021. Intrinsic elastic anisotropy of Westerly granite observed by ultrasound measurements, microstructural investigations, and neutron diffraction. J. Geophys. Res. Solid Earth 126, e2020JB020878. https://doi.org/10.1029/2020JB020878.
Lutterotti, L., Matthies, S., Wenk, H.-R., Schultz, A.J., Richardson, J.W., 1997. Combined texture and structure analysis of deformed limestone from time-of-flight neutron diffraction spectra. J. Appl. Phys. 81, 594–600. https://doi.org/10.1063/1.364220.
Lutterotti, L., Vasin, R., Wenk, H.-R., 2014. Rietveld texture analysis from synchrotron diffraction images. I. Calibration and basic analysis. Powder Diffr. 29, 76–84. https://doi.org/10.1017/S0885715613001346.
Makarynska, D., Gurevich, B., Ciz, R., Arns, C.H., Knackstedt, M.A., 2008. Finite element modelling of the effective elastic properties of partially saturated rocks. Comput. Geosci. 34, 647–657.
March, A., 1932. Mathematische Theorie der Regelung nach der Korngestalt bei affiner Deformation. Z. Kristallogr. 81, 285–297.
Martínez Catalán, J.R., Hacar Rodríguez, M.P., Villar Alonso, P., Pérez-Estaún, A., González Lodeiro, F., 1992. Lower paleozoic extensional tectonics in the limit between the West Asturian-Leonese and central iberian zones of the variscan fold-belt in NW Spain. Geol. Rundsch. 81, 545–560.
Martínez Catalán, J.R., Rubio Pascual, F.J., Montes, A.D., Fernández, R.D., Gomez Barreiro, J., Dias Da Silva, Í., Clavijo, E.G., Ayarza, P., Alcock, J.E., 2014. The late Variscan HT/LP metamorphic event in NW and Central Iberia: relationships to crustal thickening, extension, orocline development and crustal evolution. In: Schulmann, K., Martínez Catalán, J.R., Lardeaux, J.M., Janousek, V., Oggiano, G. (Eds.), The Variscan Orogeny: Extent, Timescale and the Formation of the European Crust, vol. 405. Geol. Soc. London Spec. Pub., London, pp. 225–247.
Matthies, S., 2010. On the combination of self-consistent and geometric mean elements for the calculation of the elastic properties of textured multi-phase samples. Solid State Phenom. 160, 87–93.
Matthies, S., 2012. GEO-MIX-SELF calculations of the elastic properties of a textured graphite sample at different hydrostatic pressures. J. Appl. Crystallogr. 45, 1–16.
Matthies, S., Vinel, G.W., 1982. On the reproduction of the orientation distribution function of texturized samples from reduced pole figures using the conception of a conditional ghost correction. Phys. Status Solidi 112, K111–K114.
Matthies, S., Humbert, M., 1995. On the principle of a geometric mean of even-rank symmetric tensors for textured polycrystals. J. Appl. Crystallogr. 28, 254–266.
Matthies, S., Priesmeyer, H.G., Daymond, M.R., 2001. On the diffractive determination of single-crystal elastic constants using polycrystalline samples. J. Appl. Crystallogr. 34, 585–601.
Matthies, S., Wenk, H.-R., 2009. Transformations for monoclinic crystal symmetry in texture analysis. J. Appl. Crystallogr. 42, 564–571. https://doi.org/10.1107/S0021889809018172.
Means, W.D., 1981. The concept of steady-state foliation. Tectonophysics 78 (1–4), 179–199. https://doi.org/10.1016/0040-1951(81)90013-5.
Menegon, L., Pennacchioni, G., Heilbronner, R., Pittarello, L., 2008. Evolution of quartz microstructure and c-axis crystallographic preferred orientation within ductilely deformed granitoids (Arolla Unit, Western Alps). J. Struct. Geol. 30 (11), 1332–1347. https://doi.org/10.1016/j.jsg.2008.07.007.
Minato, H., Takano, Y., 1952. On the iron sericites and magnesium sericite from Unnan Mine, Shimane Prefecture, Japan. College General Education, Univ. Tokyo Sci. Papers 2, 189.
Minor, A., Rybacki, E., Sintubin, M., Vogel, S., Wenk, H.-R., 2018. Tracking mechanical Dauphiné twin evolution with applied stress in axial compression experiments on a low-grade metamorphic rock. J. Struct. Geol. 112, 81–94. https://doi.org/10.1016/j.jsg.2018.04.002.
Mookherjee, M., Mainprice, D., 2014. Unusually large shear wave anisotropy for chlorite in subduction zone settings. Geophys. Res. Lett. 41, 1506–1513.
Morris, A.P., 1981. Competing deformation mechanisms and slaty cleavage in deformed, quartzose meta-sediments. J. Geol. Soc. London 138 (4), 455–462. https://doi.org/10.1144/gsjgs.138.4.0455.
Morris, P.R., 1970. Elastic constants of polycrystals. Int. J. Eng. Sci. 8, 49–61.
Nye, J.F., 1985. The Physical Properties of Crystals: Their Representation by Tensors and Matrices. Oxford University Press, Oxford, p. 330.
Oertel, G., 1983. The relationship of strain and preferred orientation of phyllosilicate grains in rocks-a review. Tectonophysics 100, 413–447. https://doi.org/10.1016/0040-1951(83)90197-X.
Oertel, G., Curtis, C.D., 1972. Clay ironstone concretion preserving fabrics due to progressive compaction. Geol. Soc. Am. Bull. 83, 2597–2606. https://doi.org/10.1130/0016-7606(1972)83[2597:CCPFDT]2.0.CO;2.
Oertel, G., Curtis, C.D., Phakey, P.P., 1973. A transmission electron microscope and x-ray diffraction study of muscovite and chlorite. Mineral. Mag. 39, 176–188. https://doi.org/10.1180/minmag.1973.039.302.05.
Oertel, G., Phakey, P.P., 1972. The texture of a slate from nantlle, caernarvon, North wales. Texture 1, 1–8. https://doi.org/10.1155/TSM.1.1.
Pabst, A., 1931. „Pressure-Shadows" and the measurement of the orientation of minerals in rocks. Am. Mineral. 16, 55–70.
Palomeras, I., Ayarza, P., Andrés, J., Álvarez-Valero, A.M., Gómez-Barreiro, J., Díaz, J., Alcalde, J., Carbonell, R., 2021. Mapping and interpreting the uppermost mantle reflectivity beneath central and south-west Iberia. J. Geophys. Res. 126, e2020JB019987.
Passchier, C.W., Trouw, R.A.J., 2005. Microtectonics, second ed. Springer, ISBN 978-3-540-29359-0.
Paterson, M.S., 1973. Nonhydrostatic thermodynamics and its geologic applications. Rev. Geophys. Space Phys. 11, 355–389.
Pérez-Estaún, A., Martinez-Catalán, J.R., Bastida, F., 1991. Crustal thickening and deformation sequence in the footwall to the suture of the Variscan belt of northwest Spain. Tectonophysics 191, 243–253.
Plessmann, W. Von, 1964. Gesteinslösung, ein Hauptfaktor beim Schieferungsprozess. Geol. Mitt. Aachen 4, 69–82.
Plessmann, W. Von, 1966. Lösung, Verformung, Transport und Gefüge. Z. Dtsch. Geol. Ges. 115, 650–663.
Popa, N.C., 1998. The (hkl) dependence of diffraction-line broadening caused by strain and size for all Laue groups in Rietveld refinement. J. Appl. Crystallogr. 31, 176–180.
Reuss, A., 1929. Berechnung der Fließgrenze von Mischkristallen auf Grund der Plastizitätsbedingung für Einkristalle. Z. Angew. Math. Mech. 9, 49–58.
Rietveld, H.M., 1969. A profile refinement method for nuclear and magnetic structures. J. Appl. Crystallogr. 2, 65–71. https://doi.org/10.1107/S0021889869006558.
Ruiz, M., Diaz, J., Pedreira, D., Gallart, J., Pulgar, J.A., 2017. Crustal structure of the North Iberian continental margin from seismic refraction/wide-angle reflection profiles. Tectonophysics 717, 65–82.
Rutter, E.H., 1976. The kinetics of rock deformation by pressure solution. Phil. Trans. Roy. Soc. Lond. 283, 203–219. https://doi.org/10.1098/rsta.1976.0079.
Shimizu, I., 2001. Nonequilibrium thermodynamics of nonhydrostatically stressed solids. In: Teisseyre, Roman, Majewski, Eugeniusz (Eds.), Earthquake Thermodynamics and Phase Transformation in the Earth's Interior. Academic Press, pp. 81–102. https://doi.org/10.1016/S0074-6142(01)80079-6.
Siddans, A.W.B., 1972. Slaty cleavage: a review of research since 1815. Earth Sci. Rev. 8 (2), 205–212.
Sintubin, M., 1994. Phyllosilicate preferred orientation in relation to strain path determination in the lower Paleozoic Stavelot-Venn Massif (Ardennes, Belgium). Tectonophysics 237, 215–231. https://doi.org/10.1016/0040-1951(94)90256-9.

Sorby, H.C., 1853. On the origin of slaty cleavage. New Philos. J. (Edinburgh) 55, 137–148.
Sorby, H.C., 1856. On the theory of the origin of slaty cleavage. Phil. Mag. 12, 127–129.
Srisutthiyakorn, N., Hunter, S., Sarker, R., Hofmann, R., Espejo, I., 2018. Predicting elastic properties and permeability of rocks from 2D thin sections. Lead. Edge 37, 402–480.
Suárez-Ruiz, I., Flores, D., Graciano Mendonça Filho, J., Hackley, P.C., 2012. Review and update of the applications of organic petrology: Part 1, geological applications. Int. J. Coal Geol. 99, 54–112.
Suchy, V., Sykorova, I., Melka, K., Filip, J., Machovic, V., 2007. Illite 'crystallinity', maturation of organic matter and microstructural development associated with lowest-grade metamorphism of Neoproterozoic sediments in the Tepla-Barrandian unit, Czech Republic. Clay Miner. 42 (4), 503–526.
Tillman, K.S., Byrne, T.B., 1995. Kinematic analysis of the Taiwan slate belt. Tectonics 14 (2), 322–341.
Toy, V.G., Prior, D.J., Norris, R.J., 2008. Quartz fabrics in the Alpine Fault mylonites: influence of pre-existing preferred orientations on fabric development during progressive uplift. J. Struct. Geol. 30 (5), 602–621. https://doi.org/10.1016/j.jsg.2008.01.001.
Turnbull, I.M., Mortimer, N., Craw, D., 2001. Textural zones in the haast schist—a reappraisal, New Zealand. J. Geol. Geophys. 44 (1), 171–183. https://doi.org/10.1080/00288306.2001.9514933.
Ulian, G., Moro, D., Valdre, G., 2018. First principle investigation of the mechanical properties of natural layered nanocomposite: clinochlore as a model system for heterodesmic structures. Compos. Struct. 202, 551–558.
Valcke, S.L.A., Casey, M., Lloyd, G.E., Kendall, J.-M., Fisher, Q.J., 2006. Lattice preferred orientation and seismic anisotropy in sedimentary rocks. Geophys. J. Int. 166, 652–666. https://doi.org/10.1111/j.1365-246X.2006.02987.x.
van Norden, M., Sintubin, M., Darboux, J.-R., 2007. Incipient strain partitioning in a slate belt: evidence from the early Variscan Monts d'Arrée slate belt (Brittany, France). J. Struct. Geol. 29 (5), 837–849.
Vasin, R., Wenk, H.-R., Kanitpanyacharoen, W., Matthies, S., Wirth, R., 2013. Anisotropy of Kimmeridge shale. J. Geophys. Res. 118, 1–26. https://doi.org/10.1002/jgrb.50259.
Vasin, R., Kern, H., Lokajicek, T., Svitek, T., Lehmann, E., Mannes, D.C., Chaouche, M., Wenk, H.-R., 2017. Elastic anisotropy of Tambo gneiss from Promontogno, Switzerland: a comparison of crystal orientation and microstructure-based modeling and experimental measurements. Geophys. J. Int. 209, 1–20. https://doi.org/10.1093/gji/ggw487.
Vaughan, M.T., Guggenheim, S., 1986. Elasticity of muscovite and its relationship to crystal structure. J. Geophys. Res. 91, 4657–4664. https://doi.org/10.1029/JB091iB05p04657.
Vernik, L., Liu, X., 1997. Velocity anisotropy in shales: a petrophysical study. Geophysics 62, 521–532. https://doi.org/10.1190/1.1444162.
Voigt, W., 1887. Theoretische Studien über die Elastizitätsverhältnisse der Krystalle. Dieterichsche Verlags-Buchhandlung, Göttingen, p. 100.
Voltolini, M., Wenk, H.-R., Mondol, N.H., Bjørlykke, K., Jahren, J., 2009. Anisotropy of experimentally compressed kaolinite-illite-quartz mixtures. Geophysics 74, D13–D23. https://doi.org/10.1190/1.3002557.
Wagner, W., 2007. The basics of test methods of slates for roofing and cladding. Grundlagen für die Prüfung von Dach- und Wandschiefern. Z. Dtsch. Ges. Geowiss. 158, 785–805.
Weber, K., 1981. Kinematic and metamorphic aspects of cleavage formation in very low-grade metamorphic slates. Tectonophysics 78, 291–306. https://doi.org/10.1016/0040-1951(81)90018-4.
Wenk, H.-R., 1998. Pole figure measurements with diffraction techniques. In: Kocks, U. F., Tomé, C.N., Wenk, H.-R. (Eds.), Texture and Anisotropy. Cambridge University Press (Chapter 4).
Wenk, H.-R., Matthies, S., Donovan, J., Chateigner, D., 1998. BEARTEX: a Windows-based program system for quantitative texture analysis. J. Appl. Crystallogr. 31, 262–269. https://doi.org/10.1107/S002188989700811X.
Wenk, H.-R., Voltolini, M., Kern, H., Popp, H., Mazurek, M., 2008. Anisotropy of Mont Terri opalinus clay. Lead. Edge 27, 742–748.
Wenk, H.-R., Kanitpanyacharoen, W., Voltolini, M., 2010. Preferred orientation of phyllosilicates: comparison of fault gouge, shale and schist. J. Struct. Geol. 32, 478–489. https://doi.org/10.1016/j.jsg.2010.02.003.
Wenk, H.-R., Vasin, R.N., Kern, H., Matthies, S., Vogel, S.C., Ivankina, T.I., 2012. Revisiting elastic anisotropy of biotite gneiss from the Outokumpu scientific drill hole based on new texture measurements and texture-based velocity calculations. Tectonophysics 570–571, 123–134. https://doi.org/10.1016/j.tecto.2012.06.023.
Wenk, H.-R., Lutterotti, L., Kaercher, P., Kanitpanyacharoen, W., Miyagi, L., Vasin, R., 2014. Rietveld texture analysis from synchrotron diffraction images: II. Complex multiphase materials and diamond anvil cell experiments. Powder Diffr. 29, 220–232. https://doi.org/10.1017/S0885715614000360.
Wenk, H.-R., Kanitpanyacharoen, W., Ren, Y., 2019. Slate – a new record for crystal preferred orientation. J. Struct. Geol. 125 (50), 319–324. https://doi.org/10.1016/j.jsg.2017.12.009 year special issue.
Wenk, H.-R., Yu, R., Cardenes, V., Lopez-Sanchez, M.A., Sintubin, M., 2020. Review: fabric and anisotropy of slates: from classical studies to new results. J. Struct. Geol. 138, 104066 https://doi.org/10.1016/j.jsg.2020.104066.
Weyl, P.K., 1959. Pressure solution and force of crystallisation-A phenomenological theory. J. Geophys. Res. 64 (11), 2001–2025. https://doi.org/10.1029/JZ064i011p02001.
White, S.H., Knipe, R.J., 1978. Microstructure and cleavage development in selected slates. Contrib. Mineral. Petrol. 66 (2), 165–174. https://doi.org/10.1007/BF00372155.
Williams, P.F., 1977. Relationship between axial plane foliation and strain. Tectonophysics 30, 181–196.
Winter, J.K., Ghose, S., Okamura, F.P., 1977. A high-temperature study of the thermal expansion and the anisotropy of the sodium atom in low albite. Am. Mineral. 62, 921–931.
Wood, D.S., 1974. Current views of the development of slaty cleavage. Ann. Rev. Earth. Sci. 2, 1–35.
Wood, D.S., Oertel, G., Singh, J., Bennett, H.F., 1976. A discussion of natural strain and geological structure - strain and anisotropy in rocks. Phil. Trans. Roy. Soc. Lond. 283, 27–42. https://doi.org/10.1098/rsta.1976.0067.
Wood, D.S., Oertel, G., 1980. Deformation in the cambrian slate belt of wales. J. Geol. 88 (3), 309–326.
Wright, T.O., Platt, L.B., 1982. Pressure dissolution and cleavage in the martinsburg shale. Am. J. Sci. 282 (2), 122–135. https://doi.org/10.2475/ajs.282.2.122.
Zanazzi, P.F., Comodi, P., Nazzareni, S., Andreozzi, G.B., 2009. Thermal behaviour of chlorite: an in situ single-crystal and powder diffraction study. Eur. J. Mineral 21, 581–589.
Zhong, X., Frehner, M., Kunze, K., Zappone, A., 2014. A novel EBSD-based finite-element wave propagation model for investigating seismic anisotropy: application to Finero Peridotite, Ivrea-Verbano Zone, Northern Italy. Geophys. Res. Lett. 41, 7105–7114.